Structural Engineering and Mechanics, *Vol. 63, No. 3 (2017) 329-345*
DOI: https://doi.org/10.12989/sem.2017.63.3.329

Study on dynamic interaction between crack and inclusion or void by using XFEM

Shouyan Jiang* and Chengbin Du[a]

Department of Engineering Mechanics, Hohai University, Nanjing 210098, China

(Received October 25, 2016, Revised February 24, 2017, Accepted March 30, 2017)

Abstract. This paper devoted to study dynamic interaction between crack and inclusion or void by developing the eXtended Finite Element Methods (XFEM). A novel XFEM approximation is presented for these structures containing multi discontinuities (void, inclusion, and crack). The level set methods are used so that elements that include a crack segment, the boundary of a void, or the boundary of an inclusion are not required to conform to discontinuous edges. The investigation covers the effects of a single circular or elliptical void / stiff inclusion, and multi stiff inclusions on the crack propagation path under dynamic loads. Both the void and the inclusion have a significant effect on the dynamic crack propagation path. The crack initially curves towards into the void, then, the crack moves round the void and propagates away the void. If a large void lies in front of crack tip, the crack may propagate into the void. If an enough small void lies in front of crack tip, the void may have a slight or no influence on the crack propagation path. For a stiff inclusion, the crack initially propagates away the inclusion, then, after the crack moves round the inclusion, it starts to propagate along its original path. As δ (the ratio of the elastic modulus of the inclusion to that of the matrix) increases, a larger curvature of the crack path deflection can be observed. However, as δ increases from 2 to 10, the curvature has an evident increase. By comparison, the curvature has a slight increase, as δ increases from 10 to 1000.

Keywords: extended finite element methods; dynamic interaction; crack; inclusion; void

1. Introduction

The composite materials, such as particle reinforced material, fiber composite material, have a wide application in engineering structures. Adding some small-sized inclusions into the matrix can largely improve the mechanical properties of these composite materials. However, some initial defects, such as cracks, voids, can also always be found in these heterogeneous materials. In the engineering fields, the occurrence of disasters caused by the development of cracks and voids, which are included in the building, is often happened. In order to better understand the mechanical behavior of heterogeneous materials, the interaction between cracks and voids or inclusions have to be investigated. Especially, it is highly worthwhile to investigate the effects of these inclusions and voids on the overall behavior (weakening or strengthening) of the product composites, in particular the cracking process which usually finally leads to the failure of the structures.

In some earlier references, most of researchers proposed some mathematical formulations for analyzing crack-inclusion interactions. Based on the Green's function solutions, Atkinson (1972) had solved the problem of the interaction between a circular inclusion and a radial crack. He had shown graphically the variation of the stress intensity factor with the distance of the crack tip from the inclusion. Erdogan *et al*. (1974) further solved the problems by considering an arbitrarily oriented crack. In later studies, Erdogan and Gupta (1975) analyzed a more complicated inclusion problem with a crack crossing the boundary. Patton and Santare (1990) analyzed the effect of a rigid elliptical inclusion on a straight crack. By distributing dislocations along the crack lines and forces along the matrix-inclusion interfaces, Lam *et al*. (1992) proposed a set of coupled integral equations for the analysis of the interaction between cracks and inclusions. Lee *et al.* (2001) used a displacement integral equation technique to tackle an unbounded elastic solid with orthotropic inclusions and voids as well as multiple inclusions and crack interaction problems. Dong *et al*. (2003) proposed a general-purpose integral formulation for the analysis of the interaction between the inclusions of arbitrary shapes and cracks. However, these formulations can only be used to deal with some quite simple problems with simple load conditions.

In numerical methods, the classical finite element methods (FEM) provide substantial capability for dealing with continuous and discontinuous problems with complicated boundary and load conditions in the engineering and scientific fields (Ortiz and Pandolfi 1999, Nishioka *et al*. 2001, Bouchard *et al*. 2003). However, for discontinuous problems, such as crack propagation problem, a refined mesh is needed near the crack tip and a continual remeshing is also performed as crack propagates. Due to an unknown crack path, the FEM is quite difficult in dealing with the modeling of arbitrary crack propagation.

*Corresponding author, Associate Professor
E-mail: syjiang@hhu.edu.cn
[a]Professor
E-mail: cbdu@hhu.edu.cn

ISSN: 1225-4568 (Print), 1598-6217 (Online)

Remeshing complicates the meshing task and is time-consuming. Subsequently, all kinds of novel numerical methods are developed for discontinuous problems, especially for crack propagation modeling, such as Element-Free Galerkin (EFG) method (Belytschko *et al*. 1994), Element-Free Particle (EFG-P) method (Rabczuk *et al*. 2004, Rabczuk *et al*. 2007, Ai and Augarde 2016), Scaled Boundary Finite Element Methods(SBFEM) (Ooi and Yang 2011, Ooi *et al*. 2012), Numerical Manifold Method (NMM) (Shi 1992, Wu and Wong 2013), Boundary Element Method (BEM) (Hattori *et al*. 2016, Simpson and Trevelyan 2011), and eXtended Finite Element Methods(XFEM). Meshless method was also widely used for fracture modeling, and recently, the method has been combined with explicit crack descriptions, again using level sets (Zhuang *et al*. 2011, Zhuang *et al*. 2012). In 2004, the cracking particle method, a simplified meshfree method, was presented for modelling of fracture (Rabczuk *et al*. 2004). Recently, Ai and Augarde (2016) proposed an adaptive cracking particle method for 2D crack propagation; the proposed method improved cracking particle method of Rabczuk in these aspects of crack path curvature modelling and efficiency for larger problems. Kumar *et al*. (2014) presented a multigrid coupled finite element and element free Galerkin approach for evaluating the fatigue life of cracked heterogeneous plate in the presence of multiple defects. Bhardwaj *et al*. (2015) presented the extended isogeometric analysis for investigating the effect of defects/flaws (holes, inclusions, cracks) on the fatigue life of functionally graded material. Among these methods, the XFEM should be one of the most promising numerical methods for the simulation of some strong and/or weak discontinuous problems.

The XFEM were first introduced by Belytschko and Black (1999), based on the idea of the partition of unity approach (Melenk and Babuška 1996). The XFEM ameliorate the drawbacks of the FEM in solving discontinuous problems by enriching the standard FEM approximation. The XFEM approximation consists of standard finite elements which are used in the major part of the domain and enriched elements in the enriched sub-domain for capturing special solution properties such as discontinuities and singularities. Therefore, the XFEM always holds these advantages. The XFEM mesh does not need to align with a discontinuity. For moving discontinuities, such as crack propagation problem, it does not need to carry on remeshing. Mesh refinement is also unnecessary around a discontinuous feature. The XFEM are quite adaptable for dealing with the coupling of strong and weak or multiple discontinuous problems. Singh *et al*. (2012) investigated the influence of the number of voids or inclusions in the domain on the stress intensity factor of the main crack. Later, Singh *et al*. (2011) evaluated the fatigue life of structures or components having multiple discontinuities, such as holes, cracks, and inclusions. Kim *et al*. (2011) analyzed the effect of equivalent initial flaw size distribution on a multiple-site damage specimen. Ye *et al*. (2012) investigated the effect of reinforcing particles on crack propagation behavior and fatigue performance during cyclic loading. Haboussa *et al*. (2011) focused on the interaction problem between cracks and holes. Sharma *et al*. (2013) studied the effect of inhomogeneities (holes, cracks, inclusions) on an edge crack by the XFEM. O'Hara *et al*. (2016) presents the application of a two-scale generalized/extended finite element method involving the interaction of multiple crack surfaces. Kumar *et al*. (2015) performed the elasto-plastic XFEM simulations to evaluate the fatigue life of plane crack problems in the presence of various defects. They also proposed a new virtual node XFEM for modeling and simulation of kinked cracks in a single element; the proposed method could be used for crack growth simulation in homogeneous and bi-materials medium (Kumar *et al*. 2015). Furthermore, their another excellent work showed the advantage of the XFEM for the evaluation of fatigue life of an edge crack plate in the presence of multiple discontinuities i.e., holes, inclusions and minor cracks (Kumar *et al*. 2015). And subsequently, they studied some new enrichment in XFEM to solved moving crack problems in bi-materials (Kumar *et al*. 2016). In our previous studies (Jiang *et al*. 2014), we studied the effects of voids or inclusions on crack propagation under static loads and on dynamic stress intensity factors by XFEM. This study is the deepening and development of our previous studies. Its aim is to investigate the effects of voids or inclusions on crack propagation under dynamic load by the implemented XFEM.

This paper is organized as follows. Section 2 discusses the level set functions of voids, inclusions, and cracks. Section 3 discusses the dynamic XFEM, including the construction of the XFEM approximation; the establishment of governing equations; the time integration scheme; and the integration schemes at the discontinuities. Section 4 describes the computation of the dynamic stress intensity factors (DSIF). Section 5 describes the crack propagation criterion. Section 6 gives several numerical examples for verifying the implemented XFEM program. Section 7 investigates the effects of a single circular or elliptical void / stiff inclusion, and multi stiff inclusions on the crack propagation path under dynamic loads. Section 8 summarises the major conclusions that can be drawn from this study.

2. Level set functions of voids, inclusions, and cracks

2.1 Level set functions of voids and inclusions

A powerful tool for tracking interfaces is the level set method (LSM) (Osher and Sethian 1988). In LSM, the interface of interest is represented as the zero level set of a function, $\phi(\boldsymbol{x})$. This function is one dimension higher than the dimension of the interface.

Consider a domain, Ω, divided into two non-overlapping subdomains, Ω^+ and Ω^-, sharing a interface, Γ, as illustrated in Fig. 1. On Ω^+, the level set function $\phi(\boldsymbol{x})>0$; on Ω^-, the level set function $\phi(\boldsymbol{x})<0$; on Γ, $\phi(\boldsymbol{x})=0$.

The circular level set function can be expressed as

$$\phi(\boldsymbol{x}) = \min_{i=1,2,...,n_c} \left\{ \left\| \boldsymbol{x} - \boldsymbol{x}_i^c \right\| - r_i^c \right\} \tag{1}$$

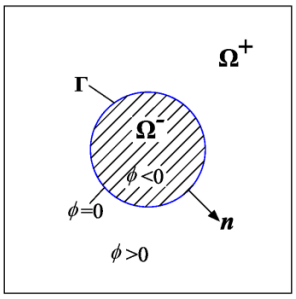

Fig. 1 Domain with a circular interface

where, n_c is the number of circular voids/inclusions, and $\boldsymbol{x}_i^{\mathrm{c}}$ is the location of the centre of the ith circular void/inclusion with the radius of r_i^{c}.

The elliptical level set function can be expressed as

$$\phi(\boldsymbol{x})=\min_{i=1,2,\ldots,n_c}\left\{\left\|\frac{\left(\left(x-x_i^{\mathrm{c}}\right)\cos\theta+\left(y-y_i^{\mathrm{c}}\right)\sin\theta\right)^2}{a^2}+\frac{\left(\left(y-y_i^{\mathrm{c}}\right)\cos\theta-\left(x-x_i^{\mathrm{c}}\right)\sin\theta\right)^2}{b^2}\right\|-1\right\} \quad (2)$$

where, n_c is the number of elliptical voids/inclusions; $\left(x_i^{\mathrm{c}},y_i^{\mathrm{c}}\right)$ is the location of the centre of the ith elliptical void/inclusion; a is the semi-major axis of the elliptical; b is the semi-minor axis of the elliptical; and θ is the orientation angle with counter clockwise, $\theta\in[-\pi,\pi]$.

In the discritized domains, the values of the level set functions are stored only at the nodes, that is $\phi_i=\phi(\boldsymbol{x}_i)$. The level set values can be interpolated over the mesh by

$$\phi^{\mathrm{h}}(\boldsymbol{x})=\sum_i N_i(\boldsymbol{x})\phi_i \quad (3)$$

where, $N_i(\boldsymbol{x})$ is the standard finite element shape functions.

2.2 Level set functions of cracks

Two level sets $\psi(\boldsymbol{x},t)$ and $\phi^k(\boldsymbol{x},t)(k=1,2)$ are used to describe the crack. As shown in Fig. 2, the functions are written as ψ and ϕ^k in the simplified form. The crack tip level set ϕ^k is generally assumed to be orthogonal to ψ. The function $\psi(\boldsymbol{x},t)$ can be expressed by the signed distance function, that is

$$\psi(\boldsymbol{x},t)=\left\|\boldsymbol{x}-\boldsymbol{x}^*\right\|\mathrm{sign}((\boldsymbol{x}-\boldsymbol{x}^*)\cdot\boldsymbol{n}) \quad (4)$$

where, $\boldsymbol{x}$ is the coordinate of the point P; $\boldsymbol{x}^*$ is the projection of the point P on the crack surface; $\boldsymbol{n}$ is the unit outward normal to the crack surface; sign(x) is the signed function; sign(x)=1 for x>0; sign(x)=0 for x=0; and sign(x)=−1 for x<0.

The function, $\phi^k(\boldsymbol{x},t)$, can be defined as

$$\phi^k(\boldsymbol{x},t)=(\boldsymbol{x}-\boldsymbol{x}_k)\cdot\boldsymbol{t} \quad (5)$$

where $\boldsymbol{x}_k$ is the coordinate of the kth crack tip and $\boldsymbol{t}$ is the unit tangential vector at the kth crack tip.

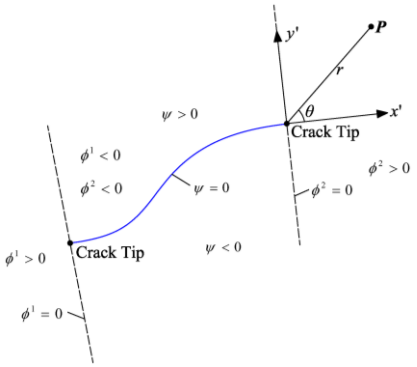

Fig. 2 Crack description by two level set functions

The values of the level set functions are stored only at the nodes as in the previous case. The level set values can be interpolated over the mesh by

$$\begin{cases}\phi^k(\boldsymbol{x},t)=\sum_i N_i(\boldsymbol{x})(\phi^k(\boldsymbol{x},t))_i\\ \psi(\boldsymbol{x},t)=\sum_i N_i(\boldsymbol{x})\psi_i(\boldsymbol{x},t)\end{cases} \quad (6)$$

Crack growth is modeled by appropriately updating the ϕ^k and ψ functions. The evolution of the level set functions ϕ^k and ψ is determined by the crack growth direction θ_c. As shown in Fig. 3, in each step, the displacement vector of the crack tip is $\boldsymbol{T}=(T_x,T_y)$. The coordinate of the crack tip CT1 is (x_1,y_1), and the coordinate of the crack tip CT2 is (x_2,y_2). The following steps describe the procedure of the evolution of the level set functions ϕ_n^k and ψ_n at the step n, that is to compute the level set functions ϕ_{n+1}^k and ψ_{n+1} at the step n+1.

Step 1: Compute the rotated level set $\phi^{k,r}$ of ϕ_n^k, and $\phi^{k,r}$ at the node with the coordinate of (x,y) can be given by

$$\phi^{k,r}=(x-x_1)\frac{T_x}{\|\boldsymbol{T}\|}+(y-y_1)\frac{T_y}{\|\boldsymbol{T}\|} \quad (7)$$

Here, the superscript 'k' of $\phi^{k,r}$ denotes the kth crack tip, and the superscript 'r' is fixed.

Step 2: Compute the level set ψ_{n+1}. If $\phi^{k,r}<0$, the level set ψ_{n+1} will not be updated, that is $\psi_{n+1}=\psi_n$. If $\phi^{k,r}>0$, ψ_{n+1} can be computed by

$$\psi_{n+1}=\pm\left|(x-x_1)\frac{T_y}{\|\boldsymbol{T}\|}+(y-y_1)\frac{T_x}{\|\boldsymbol{T}\|}\right| \quad (8)$$

Step 3: Compute the level set ϕ_{n+1}^k, and ϕ_{n+1}^k can be given by

$$\phi_{n+1}^k=\phi_n^k-\|\boldsymbol{T}\| \quad (9)$$

At a point $\boldsymbol{x}$, the polar coordinate r and θ with respect to the tangent to the crack tip are defined as

$$\begin{cases}r=\sqrt{\left[\phi^k(\boldsymbol{x},t)\right]^2+\left[\psi(\boldsymbol{x},t)\right]^2}\\ \theta=\tan^{-1}\left[\dfrac{\psi(\boldsymbol{x},t)}{\phi^k(\boldsymbol{x},t)}\right]\end{cases} \quad (10)$$

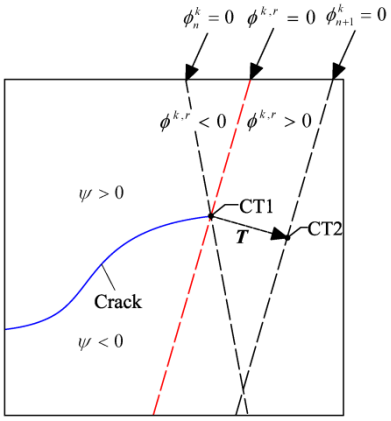

Fig. 3 Update of the level set functions

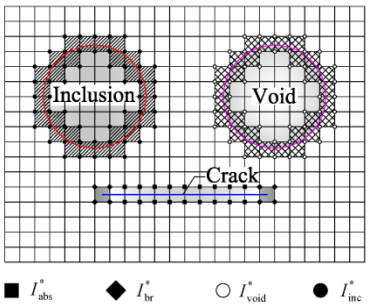

Fig. 4 Discretized domains in two dimensions with nodal subsets I^*_{abs}, I^*_{br}, I^*_{void}, and I^*_{inc}

3. Basic formulation of XFEM for dynamic problems

3.1 XFEM approximation

The XFEM approximation for 2D domains with cracks/voids/inclusions can be written as

$$\begin{aligned}\boldsymbol{u}^{\mathrm{h}}(\boldsymbol{x}) = &\sum_{i\in I} N_i(\boldsymbol{x})\boldsymbol{u}_i + \sum_{i\in I^*_{\mathrm{abs}}} N_i^*(\boldsymbol{x})[H(\boldsymbol{x}) - H(\boldsymbol{x}_i)]\boldsymbol{a}_i \\ &+ \sum_{i\in I^*_{\mathrm{br}}} N_i^*(\boldsymbol{x})\sum_{j=1}^{4}[F_j(\boldsymbol{x}) - F_j(\boldsymbol{x}_i)]\boldsymbol{b}_i^j \\ &+ \sum_{i\in I^*_{\mathrm{void}}} N_i^*(\boldsymbol{x})[V(\boldsymbol{x}) - V(\boldsymbol{x}_i)]\boldsymbol{v}_i \\ &+ \sum_{i\in I^*_{\mathrm{inc}}} N_i^*(\boldsymbol{x})[\varphi(\boldsymbol{x}) - \varphi(\boldsymbol{x}_i)]\boldsymbol{c}_i\end{aligned} \tag{11}$$

where $N_i(\boldsymbol{x})$ is the standard finite element shape function of node i; $\boldsymbol{u}_i$ is the unknown of the standard finite element part at node i; I is the set of all nodes in the domain; $N_i^*(\boldsymbol{x})$ is the partition of unity functions, and the function can hold the same form with the standard finite element shape function but are not necessarily; $\boldsymbol{a}_i$, $\boldsymbol{b}_i^j$, $\boldsymbol{v}_i$, and $\boldsymbol{c}_i$ is the nodal enriched degree of freedom; I^*_{abs}, I^*_{br}, I^*_{void}, and I^*_{inc} is the set of enrichment nodes shown in Fig. 4, and $I^*_{\mathrm{abs}}, I^*_{\mathrm{br}}, I^*_{\mathrm{void}}, I^*_{\mathrm{inc}} \subset I$.

For these elements which are cut completely by a crack, the nodes of these elements that are the nodal subset I^*_{abs} are enriched by Heaviside function $H(\boldsymbol{x})$. The definition of Heaviside function $H(\boldsymbol{x})$ follows

$$H(\boldsymbol{x}) = \begin{cases} +1, & (\boldsymbol{x} - \boldsymbol{x}^*)\cdot\boldsymbol{n} > 0 \\ -1, & (\boldsymbol{x} - \boldsymbol{x}^*)\cdot\boldsymbol{n} < 0 \end{cases} \tag{12}$$

where, $\boldsymbol{x}^*$ is the projection of a point $\boldsymbol{x}$ on the crack surface; $\boldsymbol{n}$ is the unit outward normal to the crack surface.

For these elements which are cut partially by a crack, the nodes of these elements that are the nodal subset I^*_{br} are enriched by the crack tip enrichment function $F_j(\boldsymbol{x})$. The definition of the crack tip enrichment function $F_j(\boldsymbol{x})$ follows

$$F_{j=1,2,3,4}(r,\theta) = \begin{cases} \sqrt{r}\sin(\theta/2) \\ \sqrt{r}\cos(\theta/2) \\ \sqrt{r}\sin\theta\sin(\theta/2) \\ \sqrt{r}\sin\theta\cos(\theta/2) \end{cases} \tag{13}$$

where r and θ are the local crack tip coordinate system.

For these elements which are cut by the void boundary, the nodes of these elements that are the nodal subset I^*_{void} are enriched by the function $V(\boldsymbol{x})$ (Sukumar *et al.* 2001). If the nodes lie in the void, $V(\boldsymbol{x})$=0, or else $V(\boldsymbol{x})$1.

For these elements which are cut by the inclusion interface, the nodes of these elements that are the nodal subset I^*_{inc} are enriched by the following function $\varphi(\boldsymbol{x})$

$$\varphi(\boldsymbol{x}) = \sum_{i\in I^*} N_i(\boldsymbol{x})|\phi_i| - \left|\sum_{i\in I^*} N_i(\boldsymbol{x})\phi_i\right| \tag{14}$$

It should be worth pointing out that the enrichment function $\varphi(\boldsymbol{x})$ is a ridge centered on the interface and has zero value in the blending elements (Moës *et al.* 2003). So the enrichment function can be reproduced exactly everywhere in the domain and no problems arise in the blending elements.

3.2 Governing equations

The boundary of a bounded domain, $\Omega \in R^2$, is partitioned into three parts: the displacement boundary (Γ_{u}), the traction boundary (Γ_{t}), and the crack boundary (Γ_{c}) that is traction-free. The elasto-dynamic basic equation is expressed as

$$\begin{cases} \nabla\cdot\boldsymbol{\sigma} + \boldsymbol{b} = \rho\ddot{\boldsymbol{u}} & \text{in } \Omega \\ \boldsymbol{\varepsilon} = \nabla_{\mathrm{s}}\boldsymbol{u} & \text{in } \Omega \\ \boldsymbol{\sigma} = \boldsymbol{D}:\boldsymbol{\varepsilon} & \text{in } \Omega \end{cases} \tag{15}$$

with the following boundary and initial conditions

$$\begin{cases} \boldsymbol{u}(\boldsymbol{x},t) = \bar{\boldsymbol{u}}(\boldsymbol{x},t) & \text{on } \Gamma_{\mathrm{t}} \\ \boldsymbol{\sigma}\cdot\boldsymbol{n} = \bar{\boldsymbol{t}} & \text{on } \Gamma_{\mathrm{u}} \\ \boldsymbol{\sigma}\cdot\boldsymbol{n} = 0 & \text{on } \Gamma_{\mathrm{c}} \end{cases}, \quad \begin{cases} \boldsymbol{u}(\boldsymbol{x},t=0) = \bar{\boldsymbol{u}}(0) \\ \dot{\boldsymbol{u}}(\boldsymbol{x},t=0) = \bar{\dot{\boldsymbol{u}}}(0) \end{cases} \tag{16}$$

where $\boldsymbol{\sigma}$ is the Cauchy stress tensor, $\boldsymbol{b}$ is the body force

vector, $\boldsymbol{\varepsilon}$ is the strain tensor, ρ is the material density, $\ddot{\boldsymbol{u}}$ is the acceleration field vector, ∇_s is the symmetric part of the gradient operator, $\boldsymbol{u}$ is the displacement field vector, $\boldsymbol{D}$ is the constitutive matrix, $\boldsymbol{n}$ is the unit outward normal vector to the crack surface, $\overline{\boldsymbol{u}}$ is the prescribed displacement, $\overline{\boldsymbol{t}}$ is the external traction vector, $\overline{\boldsymbol{u}}(0)$ is the initial displacement vector, and $\dot{\overline{\boldsymbol{u}}}(0)$ is the initial velocity vector.

By the principle of virtual work, the following discrete equations can be obtained

$$\boldsymbol{M}\ddot{\boldsymbol{u}}^{\mathrm{h}} + \boldsymbol{K}\boldsymbol{u}^{\mathrm{h}} = \boldsymbol{f} \tag{17}$$

where $\boldsymbol{K}(\boldsymbol{M})$ is the global stiffness(mass) matrix assembled by the element stiffness(mass) matrix; $\boldsymbol{f}$ is the global external force vector; $\boldsymbol{u}^{\mathrm{h}}$ and $\ddot{\boldsymbol{u}}^{\mathrm{h}}$ denote the vector of nodal parameters (which include the classic degrees of freedom, $\boldsymbol{u}$, and the enrichment degrees of freedom, $\boldsymbol{a}$,$\boldsymbol{b}$,$\boldsymbol{v}$,$\boldsymbol{c}$) and its second time derivative, respectively; and

$$\begin{aligned}\boldsymbol{u}^{\mathrm{h}} &= \{\boldsymbol{u},\ \boldsymbol{a},\ \boldsymbol{b},\ \boldsymbol{v},\ \boldsymbol{c}\}^{\mathrm{T}}\\ \ddot{\boldsymbol{u}}^{\mathrm{h}} &= \{\ddot{\boldsymbol{u}},\ \ddot{\boldsymbol{a}},\ \ddot{\boldsymbol{b}},\ \ddot{\boldsymbol{v}},\ \ddot{\boldsymbol{c}}\}^{\mathrm{T}}\end{aligned} \tag{18}$$

The element stiffness matrix is expressed by

$$\boldsymbol{k}^{\mathrm{e}} = \begin{bmatrix} \boldsymbol{k}^{\mathrm{uu}} & \boldsymbol{k}^{\mathrm{ua}} & \boldsymbol{k}^{\mathrm{ub}} & \boldsymbol{k}^{\mathrm{uv}} & \boldsymbol{k}^{\mathrm{uc}} \\ \boldsymbol{k}^{\mathrm{au}} & \boldsymbol{k}^{\mathrm{aa}} & \boldsymbol{k}^{\mathrm{ab}} & \boldsymbol{k}^{\mathrm{av}} & \boldsymbol{k}^{\mathrm{ac}} \\ \boldsymbol{k}^{\mathrm{bu}} & \boldsymbol{k}^{\mathrm{ba}} & \boldsymbol{k}^{\mathrm{bb}} & \boldsymbol{k}^{\mathrm{bv}} & \boldsymbol{k}^{\mathrm{bc}} \\ \boldsymbol{k}^{\mathrm{vu}} & \boldsymbol{k}^{\mathrm{va}} & \boldsymbol{k}^{\mathrm{vb}} & \boldsymbol{k}^{\mathrm{vv}} & \boldsymbol{k}^{\mathrm{vc}} \\ \boldsymbol{k}^{\mathrm{cu}} & \boldsymbol{k}^{\mathrm{ca}} & \boldsymbol{k}^{\mathrm{cb}} & \boldsymbol{k}^{\mathrm{cv}} & \boldsymbol{k}^{\mathrm{cc}} \end{bmatrix} \tag{19}$$

where

$$\boldsymbol{k}^{\mathrm{e}} = \begin{bmatrix} \boldsymbol{k}^{\mathrm{uu}} & \boldsymbol{k}^{\mathrm{ua}} & \boldsymbol{k}^{\mathrm{ub}} & \boldsymbol{k}^{\mathrm{uv}} & \boldsymbol{k}^{\mathrm{uc}} \\ \boldsymbol{k}^{\mathrm{au}} & \boldsymbol{k}^{\mathrm{aa}} & \boldsymbol{k}^{\mathrm{ab}} & \boldsymbol{k}^{\mathrm{av}} & \boldsymbol{k}^{\mathrm{ac}} \\ \boldsymbol{k}^{\mathrm{bu}} & \boldsymbol{k}^{\mathrm{ba}} & \boldsymbol{k}^{\mathrm{bb}} & \boldsymbol{k}^{\mathrm{bv}} & \boldsymbol{k}^{\mathrm{bc}} \\ \boldsymbol{k}^{\mathrm{vu}} & \boldsymbol{k}^{\mathrm{va}} & \boldsymbol{k}^{\mathrm{vb}} & \boldsymbol{k}^{\mathrm{vv}} & \boldsymbol{k}^{\mathrm{vc}} \\ \boldsymbol{k}^{\mathrm{cu}} & \boldsymbol{k}^{\mathrm{ca}} & \boldsymbol{k}^{\mathrm{cb}} & \boldsymbol{k}^{\mathrm{cv}} & \boldsymbol{k}^{\mathrm{cc}} \end{bmatrix} \tag{19}$$

$$\begin{aligned}\boldsymbol{k}^{rs} &= \int_{\Omega^{\mathrm{e}}} (\boldsymbol{B}^r)^{\mathrm{T}} \boldsymbol{D}\boldsymbol{B}^s \mathrm{d}\Omega\\ &= \int_{\Omega^{\mathrm{e}}} \begin{bmatrix} \boldsymbol{B}_1^r \\ \boldsymbol{B}_2^r \\ \boldsymbol{B}_3^r \\ \boldsymbol{B}_4^r \end{bmatrix} \boldsymbol{D} \begin{bmatrix} \boldsymbol{B}_1^s & \boldsymbol{B}_2^s & \boldsymbol{B}_3^s & \boldsymbol{B}_4^s \end{bmatrix} \mathrm{d}\Omega\end{aligned} \tag{20}$$

$(r, s = \mathrm{u,a,b,v,c})$

$$\boldsymbol{B}_i^{\mathrm{u}} = \begin{bmatrix} \dfrac{\partial N_i}{\partial x} & 0 & \dfrac{\partial N_i}{\partial y} \\ 0 & \dfrac{\partial N_i}{\partial y} & \dfrac{\partial N_i}{\partial x} \end{bmatrix}^{\mathrm{T}}, \quad i = 1,2,3,4 \tag{21}$$

$$\boldsymbol{B}_i^{\mathrm{a}} = \begin{bmatrix} \dfrac{\partial\left(N_i^* \widehat{H}\right)}{\partial x} & 0 & \dfrac{\partial\left(N_i^* \widehat{H}\right)}{\partial y} \\ 0 & \dfrac{\partial\left(N_i^* \widehat{H}\right)}{\partial y} & \dfrac{\partial\left(N_i^* \widehat{H}\right)}{\partial x} \end{bmatrix}^{\mathrm{T}} \tag{22}$$

$$\widehat{H} = H(\boldsymbol{x}) - H(\boldsymbol{x}_i), \quad i = 1,2,3,4$$

$$\boldsymbol{B}_i^{\mathrm{b}} = \begin{bmatrix} \boldsymbol{B}_1^{\mathrm{b1}} & \boldsymbol{B}_2^{\mathrm{b2}} & \boldsymbol{B}_3^{\mathrm{b3}} & \boldsymbol{B}_4^{\mathrm{b4}} \end{bmatrix}$$

$$\boldsymbol{B}_i^{\mathrm{bj}} = \begin{bmatrix} \dfrac{\partial\left(N_i^* \widehat{F}_j\right)}{\partial x} & 0 & \dfrac{\partial\left(N_i^* \widehat{F}_j\right)}{\partial y} \\ 0 & \dfrac{\partial\left(N_i^* \widehat{F}_j\right)}{\partial y} & \dfrac{\partial\left(N_i^* \widehat{F}_j\right)}{\partial x} \end{bmatrix}^{\mathrm{T}} \tag{23}$$

$$\widehat{F}_j = F_j(\boldsymbol{x}) - F_j(\boldsymbol{x}_i)$$

$$i, j = 1,2,3,4$$

$$\boldsymbol{B}_i^{\mathrm{v}} = \begin{bmatrix} \dfrac{\partial\left(N_i^* \widehat{V}\right)}{\partial x} & 0 & \dfrac{\partial\left(N_i^* \widehat{V}\right)}{\partial y} \\ 0 & \dfrac{\partial\left(N_i^* \widehat{V}\right)}{\partial y} & \dfrac{\partial\left(N_i^* \widehat{V}\right)}{\partial x} \end{bmatrix}^{\mathrm{T}} \tag{24}$$

$$\widehat{V} = V(\boldsymbol{x}) - V(\boldsymbol{x}_i), \quad i = 1,2,3,4$$

$$\boldsymbol{B}_i^{\mathrm{c}} = \begin{bmatrix} \dfrac{\partial\left(N_i^* \widehat{\varphi}\right)}{\partial x} & 0 & \dfrac{\partial\left(N_i^* \widehat{\varphi}\right)}{\partial y} \\ 0 & \dfrac{\partial\left(N_i^* \widehat{\varphi}\right)}{\partial y} & \dfrac{\partial\left(N_i^* \widehat{\varphi}\right)}{\partial x} \end{bmatrix}^{\mathrm{T}} \tag{25}$$

$$\widehat{\varphi} = \varphi(\boldsymbol{x}) - \varphi(\boldsymbol{x}_i), \quad i = 1,2,3,4$$

The element mass matrix is expressed by

$$\boldsymbol{m}^{\mathrm{e}} = \begin{bmatrix} \boldsymbol{m}^{\mathrm{uu}} & \boldsymbol{m}^{\mathrm{ua}} & \boldsymbol{m}^{\mathrm{ub}} & \boldsymbol{m}^{\mathrm{uv}} & \boldsymbol{m}^{\mathrm{uc}} \\ \boldsymbol{m}^{\mathrm{au}} & \boldsymbol{m}^{\mathrm{aa}} & \boldsymbol{m}^{\mathrm{ab}} & \boldsymbol{m}^{\mathrm{av}} & \boldsymbol{m}^{\mathrm{ac}} \\ \boldsymbol{m}^{\mathrm{bu}} & \boldsymbol{m}^{\mathrm{ba}} & \boldsymbol{m}^{\mathrm{bb}} & \boldsymbol{m}^{\mathrm{bv}} & \boldsymbol{m}^{\mathrm{bc}} \\ \boldsymbol{m}^{\mathrm{vu}} & \boldsymbol{m}^{\mathrm{va}} & \boldsymbol{m}^{\mathrm{vb}} & \boldsymbol{m}^{\mathrm{vv}} & \boldsymbol{m}^{\mathrm{vc}} \\ \boldsymbol{m}^{\mathrm{cu}} & \boldsymbol{m}^{\mathrm{ca}} & \boldsymbol{m}^{\mathrm{cb}} & \boldsymbol{m}^{\mathrm{cv}} & \boldsymbol{m}^{\mathrm{cc}} \end{bmatrix} \tag{26}$$

where

$$\begin{cases} \boldsymbol{m}^{\mathrm{uu}} = \int_{\Omega^{\mathrm{e}}} \rho\left(\boldsymbol{N}\right)^{\mathrm{T}} \boldsymbol{N} d\Omega \\ \boldsymbol{m}^{\mathrm{ua}} = \left[\boldsymbol{m}^{\mathrm{au}}\right]^{\mathrm{T}} = \int_{\Omega^{\mathrm{e}}} \rho\left(\boldsymbol{N}\right)^{\mathrm{T}} \left(\boldsymbol{N}\widehat{H}\right) d\Omega \\ \boldsymbol{m}_j^{\mathrm{ub}} = \left[\boldsymbol{m}_j^{\mathrm{bu}}\right]^{\mathrm{T}} = \int_{\Omega^{\mathrm{e}}} \rho\left(\boldsymbol{N}\right)^{\mathrm{T}} \left(\boldsymbol{N}\widehat{F}_j\right) d\Omega \\ \boldsymbol{m}^{\mathrm{uc}} = \left[\boldsymbol{m}^{\mathrm{cu}}\right]^{\mathrm{T}} = \int_{\Omega^{\mathrm{e}}} \rho\left(\boldsymbol{N}\right)^{\mathrm{T}} \left(\boldsymbol{N}\widehat{\varphi}\right) d\Omega \\ \boldsymbol{m}^{\mathrm{aa}} = \int_{\Omega^{\mathrm{e}}} \rho\left(\boldsymbol{N}\widehat{H}\right)^{\mathrm{T}} \left(\boldsymbol{N}\widehat{H}\right) d\Omega \\ \boldsymbol{m}^{\mathrm{aa}} = \int_{\Omega^{\mathrm{e}}} \rho\left(\boldsymbol{N}\widehat{H}\right)^{\mathrm{T}} \left(\boldsymbol{N}\widehat{H}\right) d\Omega \end{cases}$$

$$\begin{cases} \boldsymbol{m}_j^{\mathrm{ab}} = \left[\boldsymbol{m}_j^{\mathrm{ba}}\right]^{\mathrm{T}} = \int_{\Omega^{\mathrm{e}}} \rho \left(\boldsymbol{N}\widehat{H}\right)^{\mathrm{T}} \left(\boldsymbol{N}\widehat{F}_j\right) d\Omega \\ \boldsymbol{m}^{\mathrm{av}} = \left[\boldsymbol{m}^{\mathrm{va}}\right]^{\mathrm{T}} = \int_{\Omega^{\mathrm{e}}} \rho \left(\boldsymbol{N}\widehat{H}\right)^{\mathrm{T}} \left(\boldsymbol{N}\widehat{V}\right) d\Omega \\ \boldsymbol{m}^{\mathrm{ac}} = \left[\boldsymbol{m}^{\mathrm{ca}}\right]^{\mathrm{T}} = \int_{\Omega^{\mathrm{e}}} \rho \left(\boldsymbol{N}\widehat{H}\right)^{\mathrm{T}} \left(\boldsymbol{N}\widehat{\varphi}\right) d\Omega \\ \boldsymbol{m}_{jk}^{\mathrm{bb}} = \int_{\Omega^{\mathrm{e}}} \rho \left(\boldsymbol{N}\widehat{F}_j\right)^{\mathrm{T}} \left(\boldsymbol{N}\widehat{F}_k\right) d\Omega, \, j,k = 1,2,3,4 \\ \boldsymbol{m}_j^{\mathrm{bv}} = \left[\boldsymbol{m}_j^{\mathrm{vb}}\right]^{\mathrm{T}} = \int_{\Omega^{\mathrm{e}}} \rho \left(\boldsymbol{N}\widehat{F}_j\right)^{\mathrm{T}} \left(\boldsymbol{N}\widehat{V}\right) d\Omega \\ \boldsymbol{m}_j^{\mathrm{bc}} = \left[\boldsymbol{m}_j^{\mathrm{cb}}\right]^{\mathrm{T}} = \int_{\Omega^{\mathrm{e}}} \rho \left(\boldsymbol{N}\widehat{F}_j\right)^{\mathrm{T}} \left(\boldsymbol{N}\widehat{\varphi}\right) d\Omega \\ \boldsymbol{m}^{\mathrm{vv}} = \int_{\Omega^{\mathrm{e}}} \rho \left(\boldsymbol{N}\widehat{V}\right)^{\mathrm{T}} \left(\boldsymbol{N}\widehat{V}\right) d\Omega \\ \boldsymbol{m}^{\mathrm{vc}} = \left[\boldsymbol{m}^{\mathrm{cv}}\right]^{\mathrm{T}} = \int_{\Omega^{\mathrm{e}}} \rho \left(\boldsymbol{N}\widehat{V}\right)^{\mathrm{T}} \left(\boldsymbol{N}\widehat{\varphi}\right) d\Omega \\ \boldsymbol{m}^{\mathrm{cc}} = \int_{\Omega^{\mathrm{e}}} \rho \left(\boldsymbol{N}\widehat{\varphi}\right)^{\mathrm{T}} \left(\boldsymbol{N}\widehat{\varphi}\right) d\Omega \\ j = 1,2,3,4 \end{cases} \tag{27}$$

and

$$\boldsymbol{N} = \left[\boldsymbol{N}_1 \quad \boldsymbol{N}_2 \quad \boldsymbol{N}_3 \quad \boldsymbol{N}_4\right], \; \boldsymbol{N}_i = \begin{bmatrix} N_i & 0 \\ 0 & N_i \end{bmatrix} \tag{28}$$
$$i = 1,2,3,4$$

The element external force vector is

$$\boldsymbol{f}^{\mathrm{e}} = \left[\boldsymbol{f}^{\mathrm{u}} \quad \boldsymbol{f}^{\mathrm{a}} \quad \boldsymbol{f}^{\mathrm{b}} \quad \boldsymbol{f}^{\mathrm{v}} \quad \boldsymbol{f}^{\mathrm{c}}\right]^{\mathrm{T}} \tag{29}$$

where

$$\begin{cases} \boldsymbol{f}^{\mathrm{u}} = \int_{\Omega^{\mathrm{e}}} \boldsymbol{N}^{\mathrm{T}} \boldsymbol{b} \mathrm{d}\Omega + \int_{\Gamma_{\mathrm{t}}^{\mathrm{e}}} \boldsymbol{N}^{\mathrm{T}} \overline{\boldsymbol{t}} \mathrm{d}\Gamma \\ \boldsymbol{f}^{\mathrm{a}} = \int_{\Omega^{\mathrm{e}}} (\boldsymbol{N}^{*}\widehat{\boldsymbol{H}})^{\mathrm{T}} \boldsymbol{b} \mathrm{d}\Omega + \int_{\Gamma_{\mathrm{t}}^{\mathrm{e}}} (\boldsymbol{N}^{*}\widehat{\boldsymbol{H}})^{\mathrm{T}} \overline{\boldsymbol{t}} \mathrm{d}\Gamma \\ \boldsymbol{f}^{\mathrm{bj}} = \int_{\Omega^{\mathrm{e}}} (\boldsymbol{N}^{*}\widehat{\boldsymbol{F}}_j)^{\mathrm{T}} \boldsymbol{b} \mathrm{d}\Omega + \int_{\Gamma_{\mathrm{t}}^{\mathrm{e}}} (\boldsymbol{N}^{*}\widehat{\boldsymbol{F}}_j)^{\mathrm{T}} \overline{\boldsymbol{t}} \mathrm{d}\Gamma \\ \boldsymbol{f}^{\mathrm{v}} = \int_{\Omega^{\mathrm{e}}} (\boldsymbol{N}^{*}\widehat{\boldsymbol{V}})^{\mathrm{T}} \boldsymbol{b} \mathrm{d}\Omega + \int_{\Gamma_{\mathrm{t}}^{\mathrm{e}}} (\boldsymbol{N}^{*}\widehat{\boldsymbol{V}})^{\mathrm{T}} \overline{\boldsymbol{t}} \mathrm{d}\Gamma \\ \boldsymbol{f}^{\mathrm{c}} = \int_{\Omega^{\mathrm{e}}} (\boldsymbol{N}^{*}\widehat{\boldsymbol{\varphi}})^{\mathrm{T}} \boldsymbol{b} \mathrm{d}\Omega + \int_{\Gamma_{\mathrm{t}}^{\mathrm{e}}} (\boldsymbol{N}^{*}\widehat{\boldsymbol{\varphi}})^{\mathrm{T}} \overline{\boldsymbol{t}} \mathrm{d}\Gamma \\ j = 1,2,3,4 \end{cases} \tag{30}$$

3.3 Time integration schemes

The Newmark implicit time-integration scheme is used in dynamic analysis. Eq. (17) for a specific time $t+\Delta t$ is expressed as

$$\begin{cases} \boldsymbol{M}\ddot{\boldsymbol{u}}_{t+\Delta t} + \boldsymbol{K}\boldsymbol{u}_{t+\Delta t} = \boldsymbol{f}_{t+\Delta t} \\ \dot{\boldsymbol{u}}_{t+\Delta t} = \dot{\boldsymbol{u}}_t + (1-\gamma)\ddot{\boldsymbol{u}}_t \Delta t + \gamma \ddot{\boldsymbol{u}}_{t+\Delta t} \Delta t \\ \boldsymbol{u}_{t+\Delta t} = \boldsymbol{u}_t + \dot{\boldsymbol{u}}_t \Delta t + (1/2-\beta)\ddot{\boldsymbol{u}}_t \Delta t^2 + \beta \ddot{\boldsymbol{u}}_{t+\Delta t} \Delta t^2 \end{cases} \tag{31}$$

where $\boldsymbol{u}_t$, $\dot{\boldsymbol{u}}_t$ and $\ddot{\boldsymbol{u}}_t$ are the displacement, velocity, and acceleration vectors at time t, respectively; Δt is the time step; γ and β are parameters that can be determined to obtain integration accuracy and stability, with

$$\beta = \frac{1}{4}(1-\alpha)^2, \;\; \gamma = \frac{1}{2} - \alpha \;\; \text{and} \;\; -\frac{1}{3} \le \alpha \le 0$$

The Newmark implicit time-integration scheme is an unconditionally stable scheme. The solution stability does not dependent on the time step size. The selection of time step size depends on the solution accuracy.

Here, referring to the software ABAQUS (ABAQUS Theory Manual, Version 6.9), we set parameter α=−0.05 to remove the slight high frequency noise in the solution without having any significant effect on the meaningful, lower frequency response.

The following steps describe the prescribe integration method procedure, while neglecting the damping effects.

I. Initial calculations:

(i) Form stiffness matrix K, and mass matrix M.

(ii) Give the initial displacement vector $\boldsymbol{u}_0$ and the initial velocity vector $\dot{\boldsymbol{u}}_0$. Then, calculate the initial acceleration vector $\ddot{\boldsymbol{u}}_0$ by the equilibrium equation

$$\boldsymbol{M}\ddot{\boldsymbol{u}}_0 + \boldsymbol{K}\boldsymbol{u}_0 = \boldsymbol{f}_0 \tag{32}$$

(iii) Select a time step Δt and the parameters β and γ. Here, β=0.275625 and γ=0.55 are used. Calculate integration constants

$$\begin{cases} c_0 = \dfrac{1}{\beta \Delta t^2}, c_1 = \dfrac{\gamma}{\beta \Delta t}, c_2 = \dfrac{1}{\beta \Delta t} \\ c_3 = \dfrac{1}{2\beta} - 1, c_4 = \dfrac{\gamma}{\beta} - 1, c_5 = \Delta t \left(\dfrac{\gamma}{2\beta} - 1\right) \\ c_6 = \Delta t (1-\gamma), c_7 = \gamma \Delta t \end{cases} \tag{33}$$

(iv) Form the effective stiffness matrix $\tilde{\boldsymbol{K}}$

$$\tilde{\boldsymbol{K}} = \boldsymbol{K} + c_0 \boldsymbol{M} \tag{34}$$

II. For each time step:

(i) Calculate effective loads $\tilde{\boldsymbol{f}}_{t+\Delta t}$ at time $t+\Delta t$

$$\tilde{\boldsymbol{f}}_{t+\Delta t} = \boldsymbol{f}_{t+\Delta t} + \boldsymbol{M}\left(c_0 \boldsymbol{u}_t + c_2 \dot{\boldsymbol{u}}_t + c_3 \ddot{\boldsymbol{u}}_t\right) \tag{35}$$

(ii) Solve for the displacement vector $\boldsymbol{u}_{t+\Delta t}$ at time $t+\Delta t$

$$\tilde{\boldsymbol{K}}\boldsymbol{u}_{t+\Delta t} = \tilde{\boldsymbol{f}}_{t+\Delta t} \tag{36}$$

(iii) Calculate the acceleration vector $\ddot{\boldsymbol{u}}_{t+\Delta t}$ and the velocity vector $\dot{\boldsymbol{u}}_{t+\Delta t}$ at time $t+\Delta t$:

$$\begin{cases} \ddot{\boldsymbol{u}}_{t+\Delta t} = c_0\left(\boldsymbol{u}_{t+\Delta t} - \boldsymbol{u}_t\right) - c_2 \dot{\boldsymbol{u}}_t - c_3 \ddot{\boldsymbol{u}}_t \\ \dot{\boldsymbol{u}}_{t+\Delta t} = \dot{\boldsymbol{u}}_t + c_6 \ddot{\boldsymbol{u}}_t + c_7 \ddot{\boldsymbol{u}}_{t+\Delta t} \end{cases} \tag{37}$$

3.4 Integration schemes at the discontinuities

For these elements partitioned by the boundary of an inclusion, a void, or a crack, the ordinary Gauss quadrature rules cannot accurately calculate the integration of enrichment function. An alternative method that is dividing the enrichment element into a set of subpolygons needs to

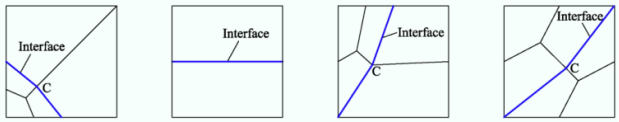

(a) Elements partitioned completely by the interface of an inclusion or a void

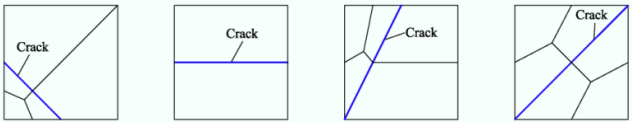

(b) Elements partitioned completely by a straight crack

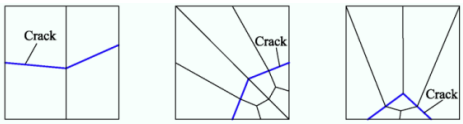

(c) Elements partitioned completely by a broken crack

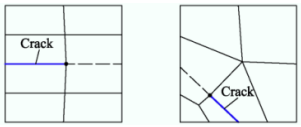

(d) Elements partitioned partially by a straight crack

Fig. 5 Element partitioning method for these elements containing a discontinuous interface

be used (Moës *et al.* 1999). In this paper, the method subdividing the element into sub-quads is used. For these elements partitioned completely or partially by the boundary of an inclusion, a void, or a crack, the method subdividing these elements into sub-quads is shown in Fig. 5. As shown in Fig. 5(a), in these elements which are partitioned completely by the interface of an inclusion or a void, the point C is computed accurately by level set function.

To solve the element stiffness or mass matrix of these enrichment elements, each sub-quad element is respectively transferred into the standard element $(-1,1)\times(-1,1)$ by the method of the coordinate transformation. The Gauss integration points are distributed into each sub-quad. The numerical integration is firstly performed in each sub-quad element domain, and then the element stiffness or mass matrix of the enrichment element can be obtained by assembling the numerical integration results of each sub-quad element. It is worthwhile pointing out that these sub-quads only necessary for integration purposes. They do not provide additional degree of freedoms for the global stiffness and mass matrix.

4. Interaction integral for computing dynamic stress intensity factors

Take field 1, $\left(\sigma_{ij}^{(1)},\varepsilon_{ij}^{(1)},u_i^{(1)}\right)$, for the actual field, and the field 2, $\left(\sigma_{ij}^{(2)},\varepsilon_{ij}^{(2)},u_i^{(2)}\right)$, for the auxiliary field. The actual field is obtained from numerical solutions computed by using XFEM, and the auxiliary field refers to the asymptotic results of linear fracture dynamics (Attigui and Petit 1997). The interaction integral equation which are used to evaluate

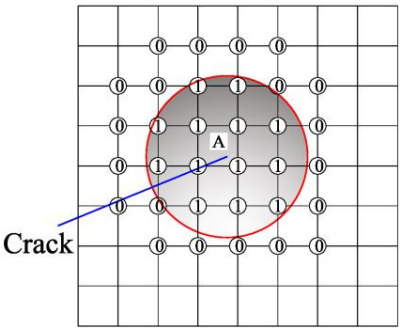

Fig. 6 Elements selection for the interaction integral near the crack tip

the DSIF follows (Song and Paulino 2006)

$$M^{(1,2)}=\int_{\mathrm{A}}\left(\sigma_{ij}^{(1)}u_{i,1}^{(2)}+\sigma_{ij}^{(2)}u_{i,1}^{(1)}-\sigma_{ik}^{(2)}\varepsilon_{ik}^{(1)}\delta_{1j}\right)\frac{\partial q}{\partial x_j}\mathrm{dA}+\int_{\mathrm{A}}\rho\ddot{u}_i^{(1)}u_{i,1}^{(2)}q\mathrm{dA} \tag{38}$$

As shown in Fig. 6, A denotes the circle domain with centre at the crack tip and the radius R. R is defined as

$$R=r_{\mathrm{k}}h_{\mathrm{e}} \tag{39}$$

where h_{e} is the crack-tip element size; r_{k} is a user-specified scalar multiple; q is the weight function; q=1 if the node lies in A; and q=0 if the node lies outside of A or lies on the boundary of A. The weight function q in the interior of an element is obtained by the interpolation of the nodal value

$$q=\sum_{i=1}^{4}N_iq_i \tag{40}$$

Additionally, the interaction integral relates to the DSIF through the relation

$$M^{(1,2)}=\frac{2}{E^*}\left[K_{\mathrm{I}}K_{\mathrm{I}}^{\mathrm{aux}}+K_{\mathrm{II}}K_{\mathrm{II}}^{\mathrm{aux}}\right] \tag{41}$$

where $K_{\mathrm{I}}^{\mathrm{aux}}$ and $K_{\mathrm{II}}^{\mathrm{aux}}$ are the local auxiliary DSIF for the auxiliary fields, respectively; and the definition of E^* is

$$E^*=\begin{cases}E & (\text{plane stress})\\ \dfrac{E}{1-\nu^2} & (\text{plane strain})\end{cases} \tag{42}$$

By setting $K_{\mathrm{I}}^{\mathrm{aux}}=1$ and $K_{\mathrm{II}}^{\mathrm{aux}}=0$ as well as $M^{(1,2)}=M_1^{(1,2)}$, we obtain the expression of K_{I} as follows

$$K_{\mathrm{I}}=E^*M_1^{(1,2)}/2 \tag{43}$$

Similarly, we obtain the equality

$$K_{\mathrm{II}}=E^*M_2^{(1,2)}/2 \tag{44}$$

by setting $K_{\mathrm{I}}^{\mathrm{aux}}=0$, $K_{\mathrm{II}}^{\mathrm{aux}}=1$, and $M^{(1,2)}=M_2^{(1,2)}$.

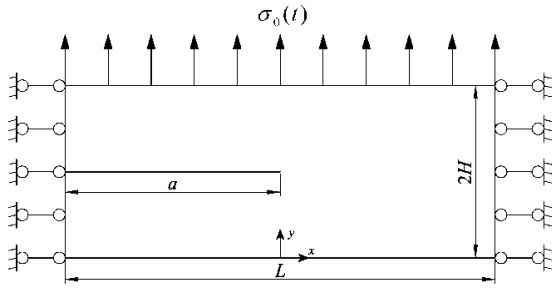

Fig. 7 Schematic of an infinite plate with a semi-infinite crack loaded by a tensile stress perpendicular to the crack surface

5. Crack propagation criteria

The maximum circumferential stress criterion (Erdogan and Sih 1963) is used to determine the crack growth direction. Once K_I and K_{II} are calculated, the criterion gives the following crack growth direction

$$\theta_c = 2\tan^{-1}\frac{1}{4}\left(\frac{K_I}{K_{II}} \pm \sqrt{\left(\frac{K_I}{K_{II}}\right)^2 + 8}\right) \tag{45}$$

where θ_c is the crack growth angle in the local crack-tip coordinate system. If K_{II}=0, then θ_c=0. It should also be noted that if K_{II}>0, the crack growth angle θ_c<0, and if K_{II}<0, then θ_c>0. By a private communication with Suo *et al.* (2003) gives an improve expression for θ_c

$$\theta_c = 2\tan^{-1}\left(\frac{-2K_{II}/K_I}{1+\sqrt{1+8\left(K_{II}/K_I\right)^2}}\right) \tag{46}$$

The equivalent stress intensity factor then follows

$$K_e = \cos\frac{\theta_c}{2}\left(K_I\cos^2\frac{\theta_c}{2} - 1.5K_{II}\sin\theta_c\right) \tag{47}$$

If $K_e \geq K_{IC}$, then the crack grows, where K_{IC} is the material's fracture toughness.

6. Numerical verification

We have implemented the corresponding XFEM program by Fortran language in the environment of Microsoft Visual Stidio 2005. In this section, we mainly give several classic examples to verify the effectiveness of the implemented XFEM program.

6.1 An infinite plate with a semi-infinite crack

The example considered in this section is an infinite plate with a semi-infinite crack loaded by a tensile stress perpendicular to the crack surface. A schematic of this problem is shown in Fig. 7. A uniform traction σ_0=500 MPa is applied to the top edge. The plate dimensions are the length L=10 m, and the width 2H=4 m. The initial crack length is a=5 m, and the vertical position of the crack is

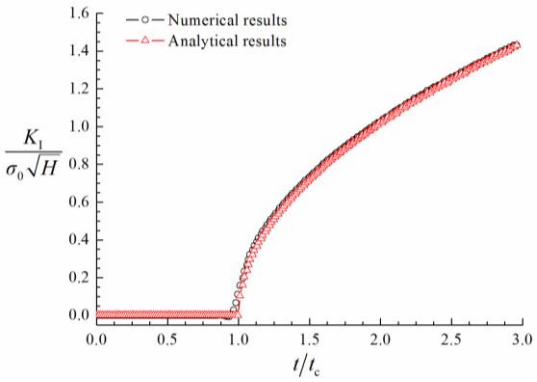

(a) Case 1

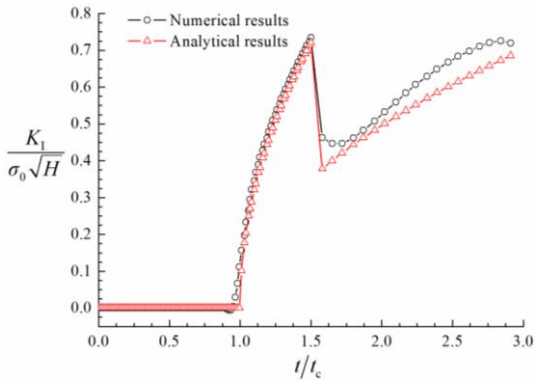

(b) Case 2

Fig. 8 Comparison of our present numerical results with theoretical solutions

H=2 m. In numerical model, the plate is discretized into 79×199 uniform mesh. Since the specimen is finite, we stop the simulation when the reflected wave from the edge reaches the crack tip, i.e., $t \leq 3t_c = 3H/c_1$ (c_1 is the dilatation wave speed). The material properties are: Young's modulus E=210 GPa, Poisson's ratio v=0.3 and the density ρ=8, 000 kg/m^3. The plane strain conditions are used.

In the problem, the Mode-I stress intensity factor for a stationary crack can be written as

$$K_I^{dyn}(0,t) = \begin{cases} 0, & t < t_c \\ \dfrac{2\sigma_0}{1-v}\sqrt{\dfrac{c_1(t-t_c)(1-2v)}{\pi}}, & t \geq t_c \end{cases} \tag{48}$$

For a moving crack, we have

$$K_I^{dyn}(\dot{a},t) = \frac{1-\dot{a}/c_r}{1-\dot{a}/(2c_r)}K_I^{dyn}(0,t) \tag{49}$$

where, the Rayleigy wave speed c_r=2, 947 m/s, and the dilatational wave speed c_1=5, 944 m/s.

This theoretical solution will be compared with our numerical results. We will investigate these cases: i) the crack does not propagate; ii) the crack initially does not propagate, and after time t=1.5t_c, the crack starts to propagate at a prescribed constant velocity $\dot{a}$=2000 m/s.

This example is pure mode-I crack problem. As shown in Fig. 8, by comparing mode-I dynamic stress intensity factor obtained from our present numerical results with that

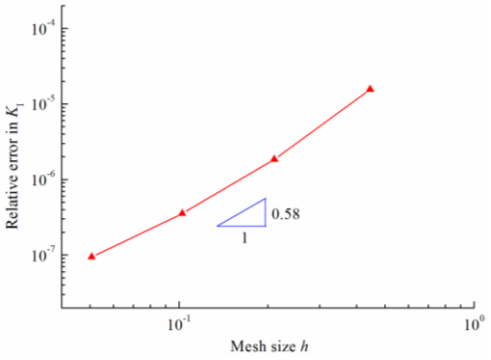

Fig. 9 Convergence curves in mode-I stress intensity factor

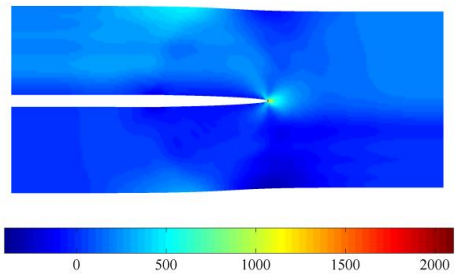

(a) x-directional displacement contour (Unit: mm)

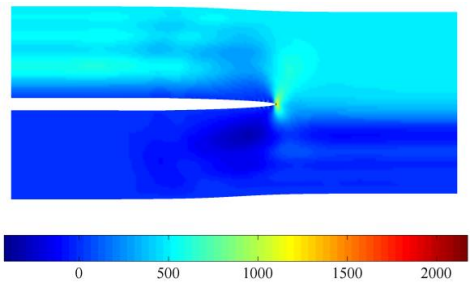

(b) y-directional displacement contour (Unit: mm)

Fig. 10 Deformed plate after the crack propagation (with 20 times magnified deformation)

obtained from theoretical solutions, a fairly satisfactory agreement can be observed.

Additionally, a convergence study of approximation accuracy is made by using following relative L_2 norm e_2

$$e_2 = \frac{\left\| \boldsymbol{K}_{\mathrm{I}}^{\mathrm{num}} - \boldsymbol{K}_{\mathrm{I}}^{\mathrm{ana}} \right\|_{L^2}}{\left\| \boldsymbol{K}_{\mathrm{I}}^{\mathrm{ana}} \right\|_{L^2}} = \left(\frac{\sum_t \left(K_{\mathrm{I}}^{\mathrm{num}} - K_{\mathrm{I}}^{\mathrm{ana}} \right)^2}{\sum_t \left(K_{\mathrm{I}}^{\mathrm{ana}} \right)^2} \right)^{1/2} \tag{50}$$

where, $K_{\mathrm{I}}^{\mathrm{num}}$ is the mode-I stress intensity factor obtained by the present numerical results; $K_{\mathrm{I}}^{\mathrm{ana}}$ is the analytical mode-I stress intensity factor.

The convergence curves for mode-I stress intensity factor for solutions obtained with different mesh sizes are shown in Fig. 9. The XFEM displays a remarkable ability for capturing the value of the stress intensity factor as the mesh is refined. We also show the deformed structure after the crack propagation given in Fig. 10 and the stress distribution in Fig. 11. Results show that the XFEM can better capture the stress singularity at the crack tip.

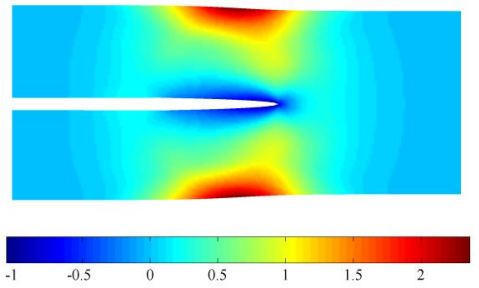

(a) Normal stress σ_{xx}

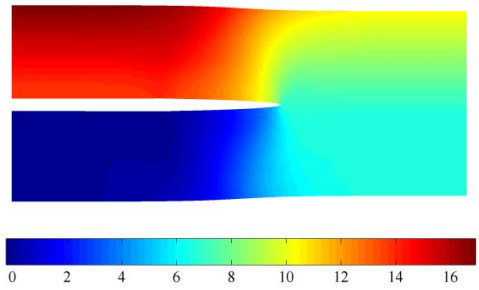

(b) Normal stress σ_{yy}

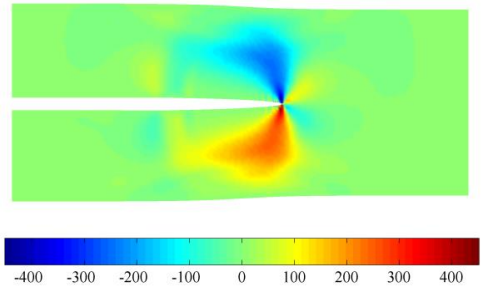

(c) Shear stress τ_{xy}

Fig. 11 Stress distribution contours after the crack propagation (Unit: MPa)

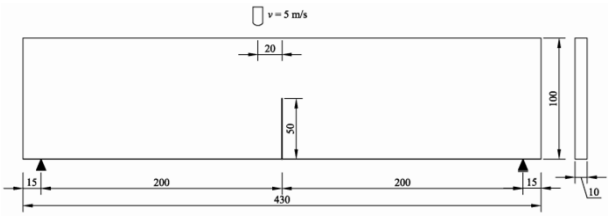

(a) Geometry and dimension(Unit: mm)

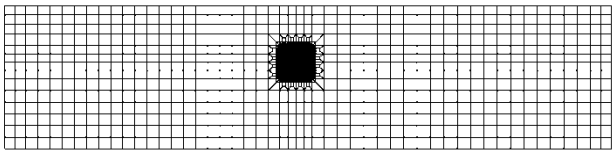

(b) XFEM mesh

Fig. 12 Impact on a notched PMMA beam

6.2 A notched Polymethlyl Methacrylate (PMMA) beam subjected to an impact load

A notched Polymethlyl Methacrylate (PMMA) beam subjected to an impact load tested by Nishioka *et al*. (2001) as shown in Fig. 12(a) is considered. The impact velocity is 5 m/s. The material properties of PMMA beam are: Young modulus E=2940 MPa, Poisson ratio v=0.3, and density

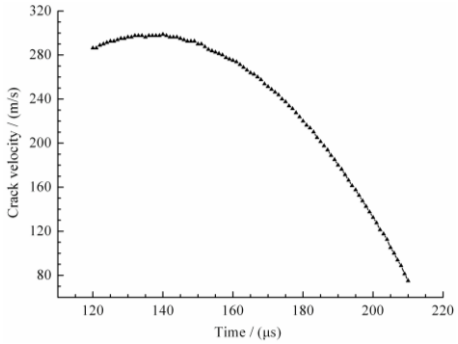

(a) Crack propagation velocity time history

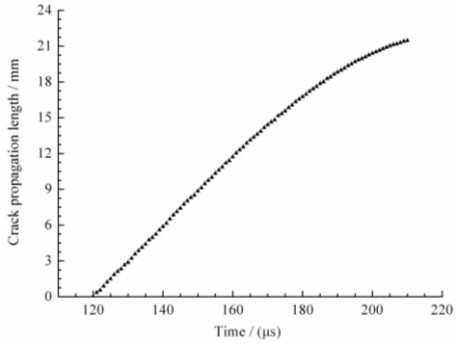

(b) Crack propagation length time history

Fig. 13 Dynamic crack propagation criterion

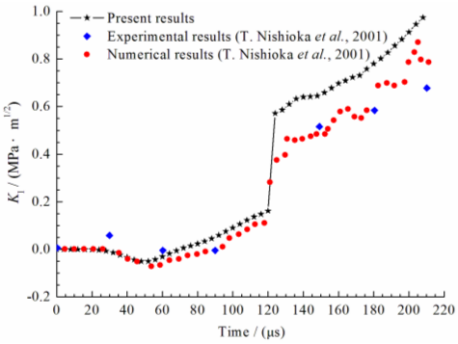

(a) Mode-I dynamic stress intensity factor

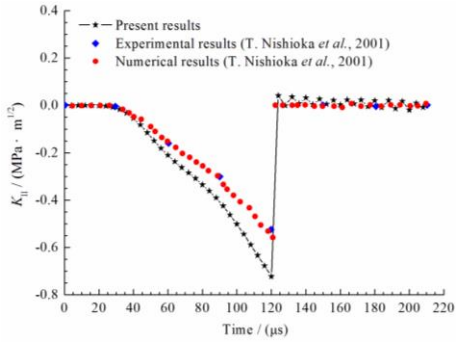

(b) Mode-II dynamic stress intensity factor

Fig. 14 Dynamic stress intensity factors time histories of the notched PMMA beam subjected to impact load

ρ=1190 kg/m^3. The thickness of the beam is 10 mm. Plane stress conditions are assumed. In numerical model, the mesh used to discretize the beam is shown in Fig. 12(b). It has 13180 elements and 13245 nodes. The crack velocity obtained from the experimental measurements shown in

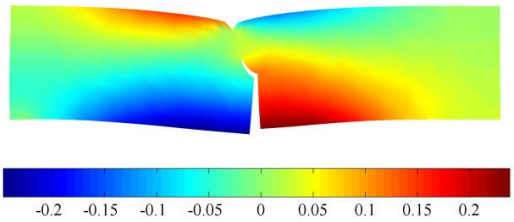

(a) x-directional displacement contour (Unit: mm)

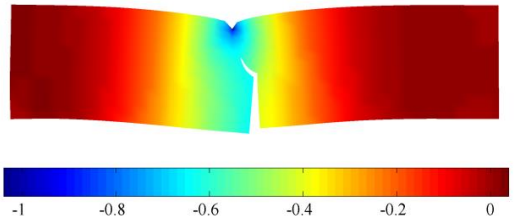

(b) y-directional displacement contour (Unit: mm)

Fig. 15 Deformed beam after the crack propagation (with 20 times magnified deformation)

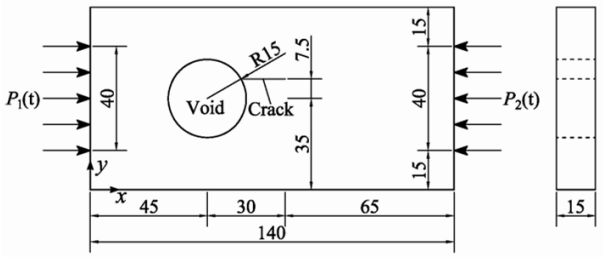

Fig. 16 Geometry and dimension of a PMMA specimen with a hole subjected to impact loads (Unit: mm)

Fig. 13 drives the crack propagation while the computed DSIF are used to predict the crack propagation direction. A time step of Δt=4 μs are used in the simulations.

This example is a mixed-mode crack problem. Fig. 14 shows a comparison for mode-I and mode-II dynamic stress intensity factors obtained from our present numerical results with that obtained from other reference's FEM simulation results (Nishioka *et al*. 2001). Although some differences in the numerical value between our present results and other reference's results can be seen, the distribution of dynamic stress intensity factors still shows a fairly satisfactory agreement. We also show the deformed structure after the crack propagation given in Fig. 15.

6.3 A PMMA specimen with a hole subjected to impact loads

A PMMA specimen with a hole (Fig. 16) subjected to impact loads at both ends is considered. Experiments on such specimens were reported by Grégoire *et al*. (2007). The material properties of the specimen are: Young modulus E=3300 MPa, Poisson ratio v=0.42 and mass density ρ=1180 kg/m^3. Plane strain conditions are assumed. As shown in Fig. 17, time dependent loads are applied to both ends of the specimen according to the BEM simulation of Fedelinski (2011). The crack is stationary between $0 \le t \le 200$ μs. It then propagates at $\dot{a}$ =210 m/s. The crack arrests between 270 μs$\le t \le$320 μs, and then propagates again

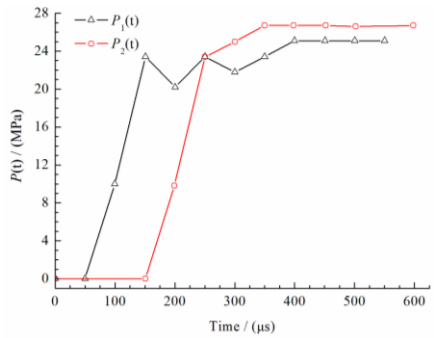

Fig. 17 Time dependent loads applied to both ends of the specimen

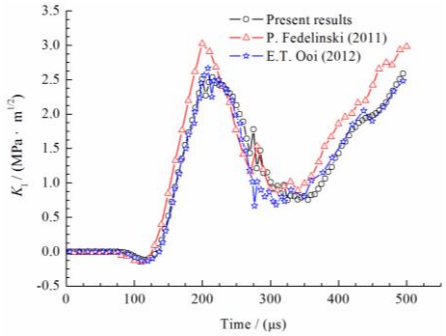

(a) Mode-I dynamic stress intensity factor

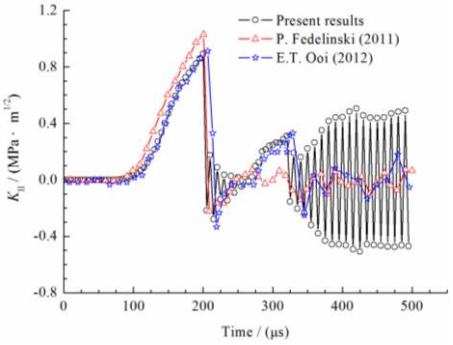

(b) Mode-II dynamic stress intensity factor

Fig. 18 Dynamic stress intensity factors time histories of notched PMMA beam with a hole subjected to impact load

at $\dot{a}$ =160 m/s until t=500 m/s. A time step of Δt=5 μs is used in the simulation. In numerical model, the plate is discretized into 90×180 uniform mesh.

As shown in Fig. 18, by comparing mode-I and mode-II DSIFs obtained from our present numerical results with that obtained from other reference's results (Fedelinski 2011, Ooi *et al*. 2012), a fairly satisfactory agreement can still be observed. We also show the deformed structure after the crack propagation given in Fig. 19.

6.4 An infinite plate with a semi-infinite crack nearby a void or an inclusion

In this example, the geometric dimension, boundary conditions, load conditions, and XFEM mesh partition both are identical with that described in Section 6.1. But here, a void or an inclusion with radius R is nearby the crack tip; see Fig. 20. The circular center coordinates of the void or

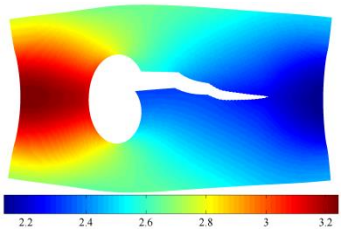

(a) x-directional displacement contour (Unit: mm)

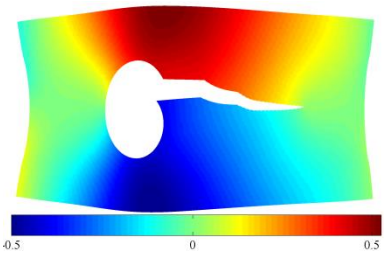

(b) y-directional displacement contour (Unit: mm)

Fig. 19 Deformed beam after the crack propagation (with 10 times magnified deformation)

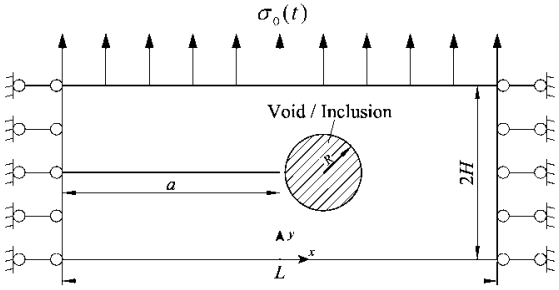

Fig. 20 Schematic of an infinite plate with a semi-infinite crack nearby a void or an inclusion

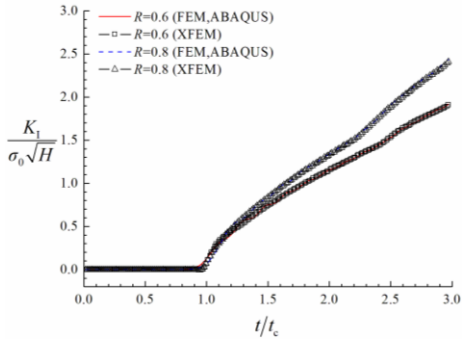

(a) A void nearby the crack tip

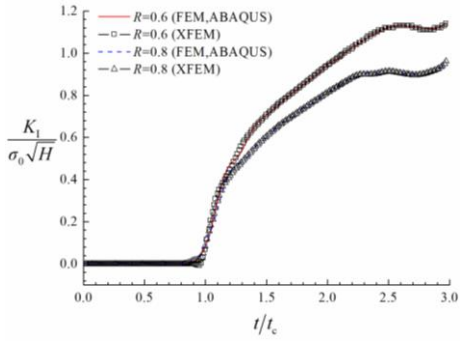

(b) An inclusion nearby the crack tip

Fig. 21 Comparison of our present numerical results with FEM solutions

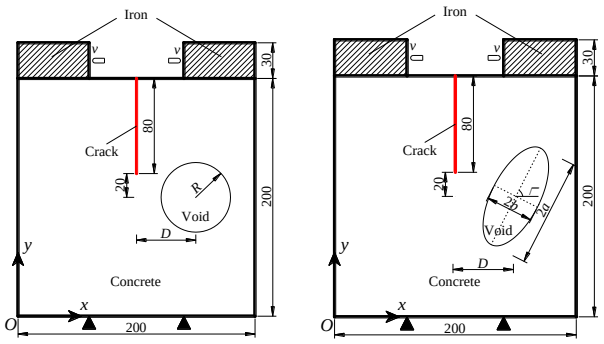

(a) With a circular void (b) With an elliptical void

Fig. 22 Schematic of a notched cubic concrete specimen with a void nearby the crack tip subjected to a splitting force (Unit: mm)

inclusion is set to (1.0, 2.0).

By this example, we examine whether the correct dynamic stress intensity factors can be obtained when a void or an inclusion is nearby the crack tip by the implemented XFEM program. As shown in Fig. 21, we compare our present numerical results with FEM solutions. The FEM solutions are obtained by the software ABAQUS. A very satisfactory agreement can be observed. This example explains the dynamic stress intensity factors can still be correctly obtained in this case when some of the inclusion node may fall into the stress intensity factors computation domain.

7. Numerical example

7.1 Crack path deflection because of a void

As shown in Fig. 22, a notched cubic concrete specimen with the dimension of 200 mm×200 mm×200 mm subjected to a splitting force is considered in this example. Additionally, a void is nearby the crack tip. We investigate the influence of the void on the crack propagation path. Here, the splitting force is applied on the iron by an impact load v=0.0893 mm/s. The iron is fastened on the concrete specimen. The material properties of concrete are: Young modulus E=28 GPa, Poisson ratio v=0.167, and mass density ρ=2400 kg/m^3. The material properties of iron are: Young modulus E=200 GPa, Poisson ratio v=0.3, and mass density ρ=7800 kg/m^3. In numerical model, the specimen is discretized into 10154 elements and 10370 nodes. The concrete material's fracture toughness K_{IC} equal to 0.64 MPa·m$^{1/2}$ tested by experiment.

As shown in Fig. 23, we investigate the dimension of the circular void on the crack propagation path. If no void lies in front of the crack tip, the crack propagates along pure mode-I crack path; see Fig. 23(a). The crack may propagate into the void if a large void ($R/D\geq0.6$) lies in front of crack tip; see Fig. 23(f), Fig. 24(e), and Fig. 25(c). The void may have a slight or no influence on the crack propagation path if an enough small void ($R/D\leq0.3$) lies in front of crack tip; see Fig. 23(b), Fig. 24(a), and Fig. 25(a). Additionally, we can observe the circular void has an obvious effect on the

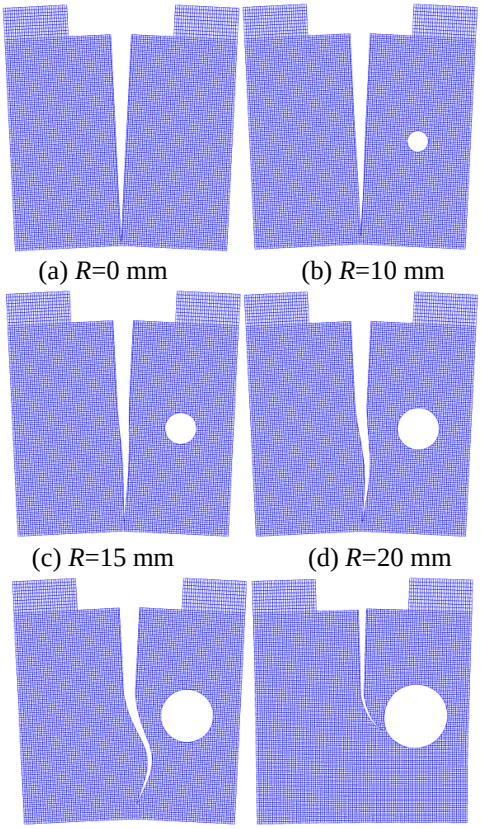

(a) R=0 mm (b) R=10 mm

(c) R=15 mm (d) R=20 mm

(e) R=25 mm (f) R=30 mm

Fig. 23 The influence of the dimension of the void on the crack propagation path (D=50 mm)

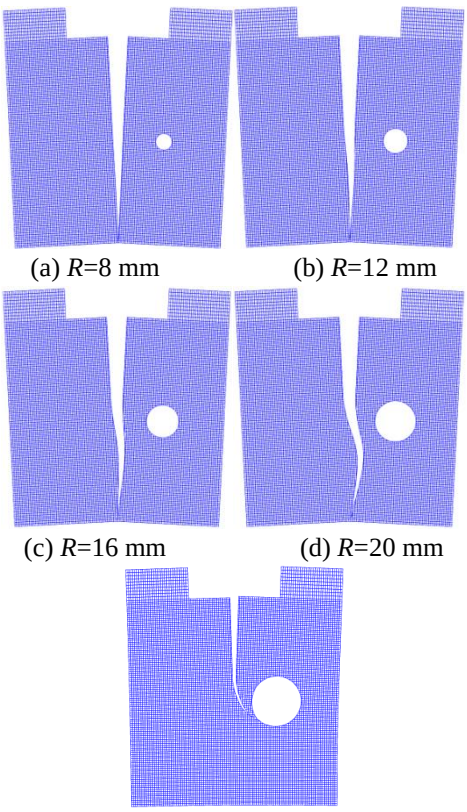

(a) R=8 mm (b) R=12 mm

(c) R=16 mm (d) R=20 mm

(e) R=24 mm

Fig. 24 The influence of the dimension of the void on the crack propagation path (D=40 mm)

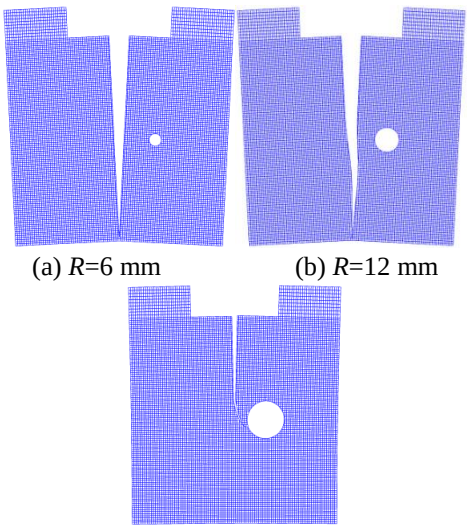

(a) R=6 mm (b) R=12 mm

(e) R=18 mm

Fig. 25 The influence of the dimension of the void on the crack propagation path (D=30 mm)

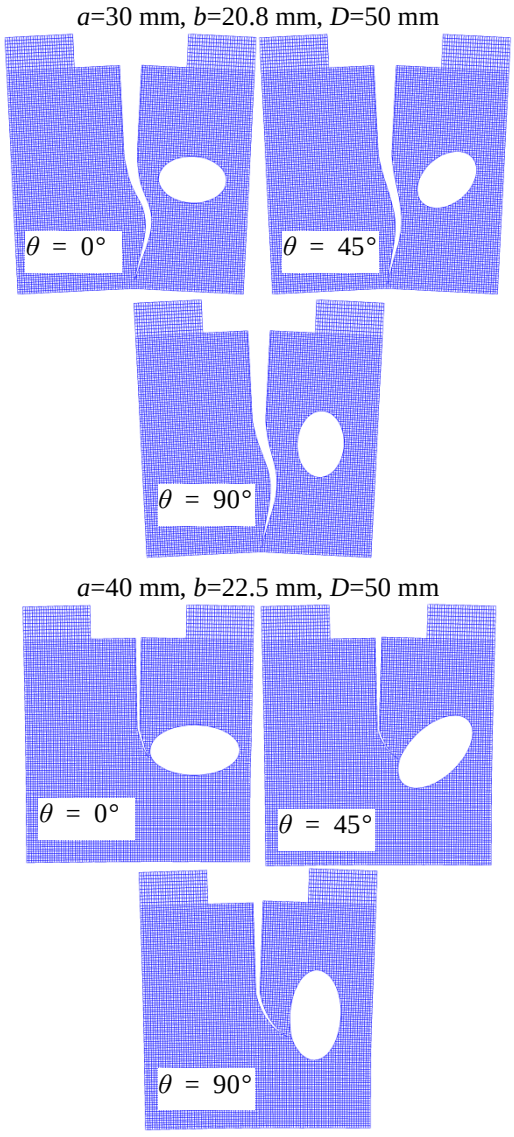

Fig. 26 The influence of the position of the elliptical void on the crack propagation path

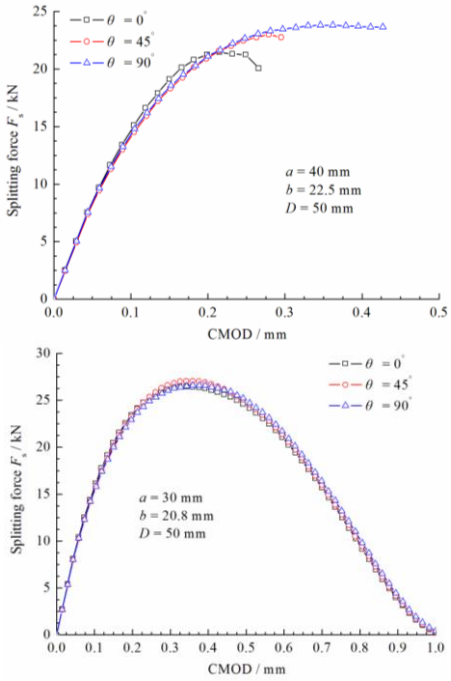

Fig. 27 Splitting force versus CMOD curve

crack path deflection when 0.3<R/D<0.6; the crack initially curves towards into the void, then, the crack moves round the void and propagates away the void.

We alter the circular void into the elliptical void at the crack tip and investigate the influence of the position of the elliptical void on the crack propagation path and fracture properties. As shown in Fig. 26, similar to the circular void, we can observe that the elliptical void with varying the orientation angle θ from 0° to 90° has an obvious effect on the crack path deflection; the crack initially curves towards into the void, then, the crack moves round the void and propagates away the void. If a large elliptical void with varying the orientation angle θ from 0° to 90° lies in front of crack tip, we also observe that the crack will propagate into the void.

As shown in Fig. 27, we can observe that the orientation angle has an obvious effect on the maximum splitting force when an enough large elliptical void lies in front of crack tip and the crack will propagate into the void. As the orientation angle θ increases, the maximum splitting force will increase. However, the orientation angle has a quite slight effect on the maximum splitting force when the crack does not propagate into the void.

7.2 Crack path deflection because of a stiff inclusion

In this section, we mainly investigate the effects of the stiff inclusion on the path of crack propagation. The geometric dimensions, material properties, the load conditions, and the boundary conditions of the plate both are identical with these described in section 7.1, but the plate contains an inclusion instead of a void. Here, the horizontal distance between the center of the inclusion and the crack tip D is set to be 50 mm. The Young's modulus (E') of the stiff inclusion varies from 56 GPa to 28000 GPa,

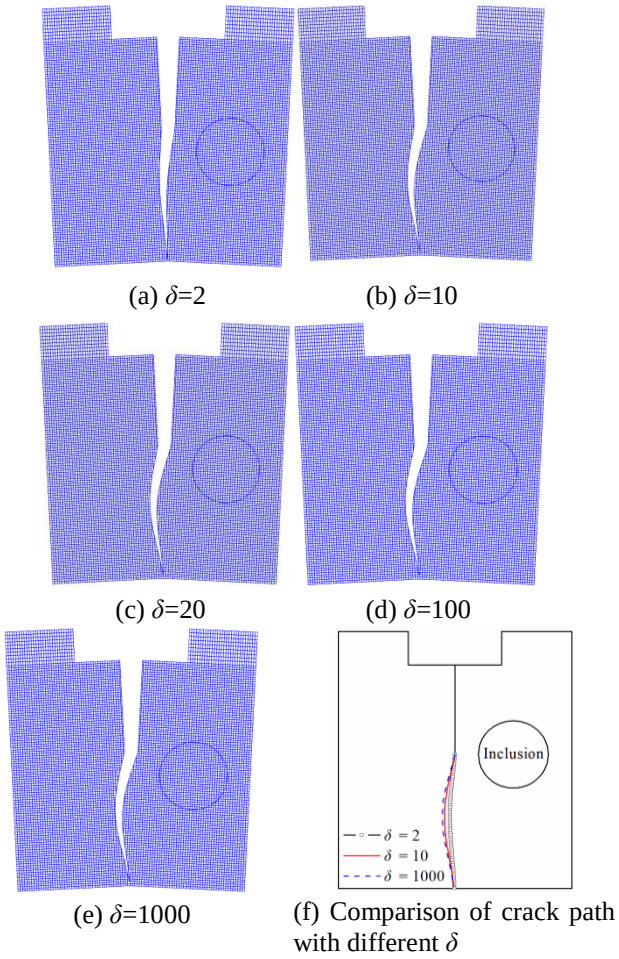

Fig. 28 The influence of the rigidity of the inclusion on the crack propagation path with δ varying from 2 to 1000

its Poisson's ratio (ν') keeps at 0.2, and mass density (ρ') 2800 kg/m^3. Defining $\delta=E'/E$, as shown in Fig. 28, we investigate the influence of the rigidity of the inclusion on the crack propagation path with δ varying from 2 to 1000. The inclusion also has an evident effect on the crack path deflection. The crack initially propagates away the inclusion, then, after the crack moves round the inclusion, it starts to propagate along its original path. As δ increases, a larger curvature of the crack path deflection can be observed. However, as δ increases from 2 to 10, the curvature has an evident increase. By comparison, the curvature has a slight increase, as δ increases from 10 to 1000; see Fig. 28(f).

As shown in Fig. 29, we also investigate the influence of the dimension of the inclusion on the crack propagation path. Here, we idealize the perfect bond interface between the inclusion and the matrix. The crack always propagates away the inclusion. Similar to the void, if an enough small inclusion ($R/D\leq0.3$) lies in front of crack tip, the inclusion will have a slight or no influence on the crack propagation path.

The orientation angle θ of the elliptical inclusion also has an evident effect on the crack path deflection. As θ decreases, a larger curvature of the crack path deflection can be observed; see Fig. 30.

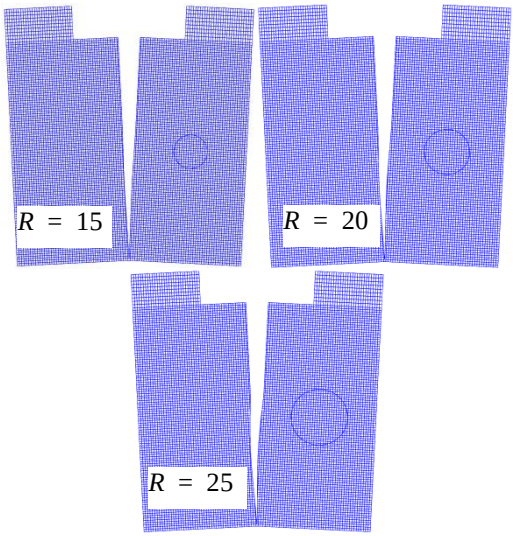

Fig. 29 The influence of the dimension of the inclusion on the crack propagation path

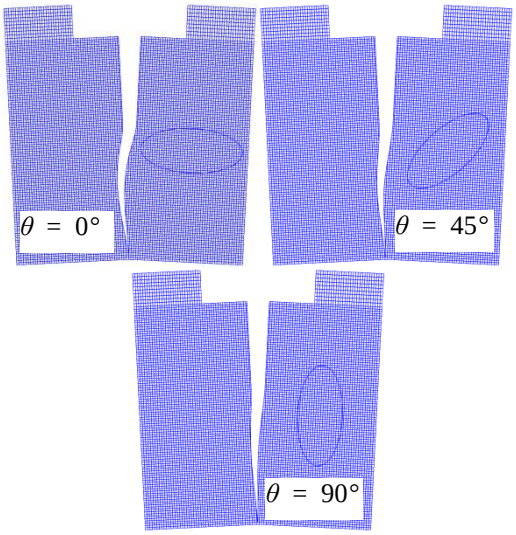

Fig. 30 The influence of the position of the elliptical inclusion on the crack propagation path

7.3 Crack path deflection because of multi stiff inclusions

In this section, we investigate the effect of the material heterogeneous on the crack propagation path deflection. Five specimens (S1, S2, S3, S4, and S5) with different inclusion distribution are generated randomly. These specimens, S1, S2, and S3, hold the same inclusion contents. The inclusion contents of the specimens, S4 and S5, are more than that of the specimens, S1, S2, and S3. As shown in Fig. 31 and Fig. 32, we can observe that the material heterogeneous has an obvious effect on the crack propagation path. When the crack encounters with a big inclusion, the crack always propagates away the inclusion or does not continue to propagate. As δ increases, a larger curvature of the crack path deflection can be observed. Additionally, from Fig. 33, we can see that the maximum splitting force will increase with the increase of the

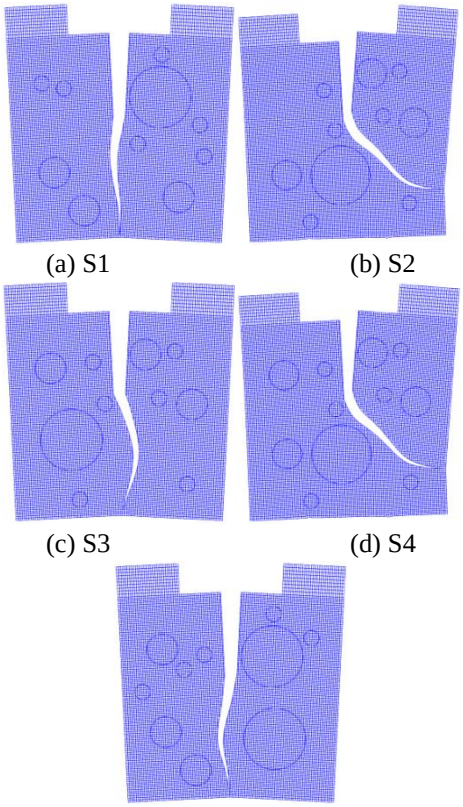

(a) S1 (b) S2

(c) S3 (d) S4

(e) S5

Fig. 31 The crack propagation path deflection due to material heterogeneous (δ=10)

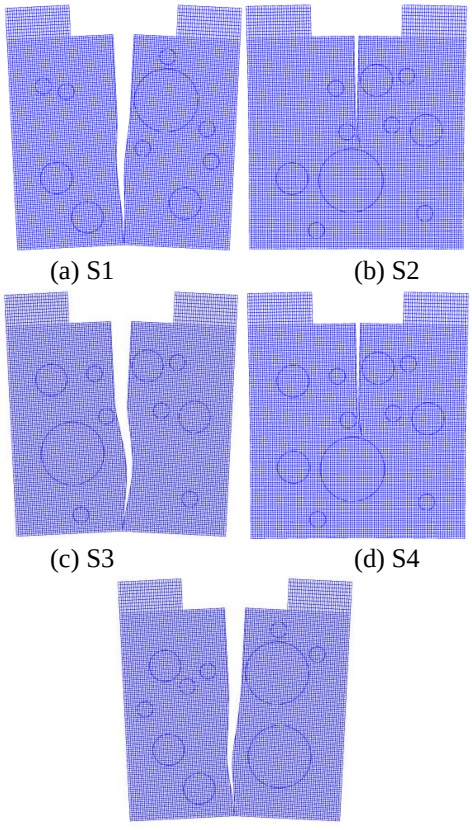

(a) S1 (b) S2

(c) S3 (d) S4

(e) S5

Fig. 32 The crack propagation path deflection due to material heterogeneous (δ=2)

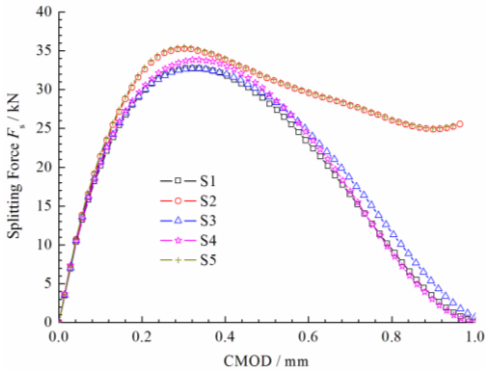

(a) δ=10

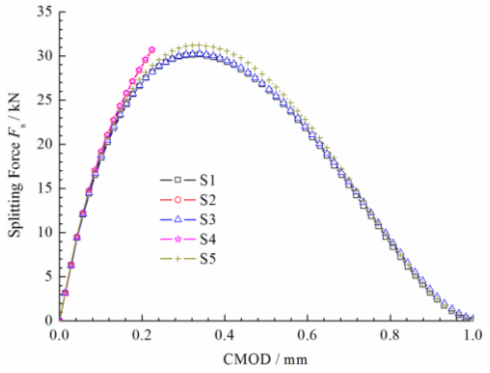

(b) δ=2

Fig. 33 Splitting force versus CMOD curve

inclusion contents. The maximum splitting force also will increase when a large inclusion lies in front of crack tip.

8. Conclusions

This paper mainly studies on dynamic interaction between crack and inclusion or void by developing XFEM. In XFEM, some basic formulations are discussed in detail, containing the selections of enrichment functions, the establishment of governing equations for dynamic XFEM, the time integration scheme, the numerical integrations at the discontinuities, the evaluations of the DSIFs, and crack propagation criterion. The level set method is used for representing the location of inner discontinuous interfaces containing the boundaries of voids and inclusions, and the surface of cracks, so that the mesh does not need to align with these discontinuities. The investigation covers the effects of a single circular or elliptical void / stiff inclusion, and multi stiff inclusions on the crack propagation path under dynamic loads. Some significant conclusions have been obtained from this study.

The circular void has a significant effect on the dynamic crack propagation path. The crack initially curves towards into the void, then, the crack moves round the void and propagates away the void. Additionally, the crack may propagate into the void if a large void lies in front of crack tip. By comparing, if an enough small void lies in front of crack tip, the void may have a slight or no influence on the crack propagation path.

Similar to the circular void, the elliptical void with

varying the orientation angle θ from 0° to 90° also has an obvious effect on the crack path deflection; the crack initially curves towards into the void, then, the crack moves round the void and propagates away the void. If a large elliptical void with varying the orientation angle θ from 0° to 90° lies in front of crack tip, we also observe that the crack will propagate into the void. In addition, the orientation angle has an obvious effect on the maximum splitting force when an enough large elliptical void lies in front of crack tip and the crack will propagate into the void. As the orientation angle θ increases, the maximum splitting force will increase. However, the orientation angle has a quite slight effect on the maximum splitting force when the crack does not propagate into the void.

The inclusion has an evident effect on the dynamic crack propagation path but it has difference compared with the void. The crack initially propagates away the inclusion, then, after the crack moves round the inclusion, it starts to propagate along its original path. As δ (the ratio of the elastic modulus of the inclusion to that of the matrix) increases, a larger curvature of the crack path deflection can be observed. However, as δ increases from 2 to 10, the curvature has an evident increase. By comparison, the curvature has a slight increase, as δ increases from 10 to 1000. The orientation angle θ of the elliptical inclusion also has an evident effect on the crack path deflection. As θ decreases, a larger curvature of the crack path deflection can be observed.

The material heterogeneous has an obvious effect on the crack propagation path. When the crack encounters with a big inclusion, the crack always propagates away the inclusion or does not continue to propagate. As δ increases, a larger curvature of the crack path deflection can be observed. Additionally, the maximum splitting force will increase with the increase of the inclusion contents. The maximum splitting force also will increase when a large inclusion lies in front of crack tip.

Acknowledgements

The authors gratefully acknowledge support for this research from the National Natural Science Foundation of China (Grant Nos. 11372098, 51309088, 51579084, 51308188, and 11132003), the Fundamental Research Funds for the Central Universities (Grant No. 2015B01714), China Postdoctoral Science Foundation funded project (Grant No. 2014T70466), and Jiangsu Province Graduate Students Research and Innovation Plan (Grant No. CXZZ130234). The authors also would like to thanks for the discussion with Prof. Charles Augarde during we visited Durham University, as well as he stayed in Hohai University supported by the Royal Society.

References

ABAQUS Theory Manual, Version 6.9.

Ai, W.L. and Augarde, C.E. (2016), "An Adaptive Cracking Particle Method for 2D Crack Propagation", *Int. J. Numer. Meth. Eng.*, **108**(13), 1626-1648.

Atkinson, C. (1972), "The interaction between a crack and an inclusion", *Int. J. Eng. Sci.*, **10**(2), 127-136.

Attigui, M. and Petit, C. (1997), "Mixed-mode separation in dynamic fracture mechanics: New path independent integrals", *Int. J. Fatigue*, **84**, 19-36.

Belytschko T. and Black, T. (1999), "Elastic crack growth in finite elements with minimal remeshing", *Int. J. Numer. Meth. Eng.*, **45**(5), 601-620.

Belytschko, T., Lu, Y.Y. and Gu, L. (1994), "Element-free Galerkin methods", *Int. J. Numer. Meth. Eng.*, **37**, 229-256.

Bhardwaj, G., Singh, I.V. and Mishra, B.K. (2015), "Fatigue crack growth in functionally graded material using homogenized XIGA", *Compos. Struct.*, **134**, 269-284.

Bouchard, P.O., Bay, F. and Chastel, Y. (2003), "Numerical modelling of crack propagation: automatic remeshing and comparison of different criteria", *Comput. Meth. Appl. Mech. Eng.*, **192**, 3887-3908.

Dong, C.Y., Lo, S.H. and Cheung, Y.K. (2003), "Numerical analysis of the inclusion-crack interactions using an integral equation", *Comput. Mech.*, **30**, 119-130.

Erdogan, F. and Gupta, G.D. (1975), "The inclusion problem with a crack crossing the boundary", *Int. J. Fracture*, **11**(1), 13-27.

Erdogan, F. and Sih, G.C. (1963), "On the crack extension in plane loading and transverse shear", *J. Basic Eng.*, **85**, 519-527.

Erdogan, F., Gupta, G.D. and Ratwani, M. (1974), "Interaction between a circular inclusion and an arbitrarily oriented crack", *J. Appl. Mech.*, **41**(4), 1007-1013.

Fedéliński, P. (2011), "Computer modelling of dynamic fracture experiments", *Key Eng. Mater.*, **454**, 113-125.

Grégoire, D., Maigre, H., Réthoré, J. and Combescure, A. (2007), "Dynamic crack propagation under mixed-mode loading-comparison between experiments and XFEM simulations", *Int. J. Solid. Struct.*, **44**, 6517-6534.

Haboussa, D., Grégoire, D., Elguedj, T., Maigre, H. and Combescure, A. (2011), "X-FEM analysis of the effects of holes or other cracks on dynamic crack propagations", *Int. J. Numer. Meth. Eng.*, **86**, 618-636.

Hattori, G., Alatawi, I.A. and Trevelyan, J. (2016), "An extended boundary element method formulation for the direct calculation of the stress intensity factors in fully anisotropic materials", *Int. J. Numer. Meth. Eng.*, **109**(7), 965-981.

Jiang, S.Y., Du, C.B. and Gu, C.S. (2014), "An investigation into the effects of voids, inclusions and minor cracks on major crack propagation by using XFEM", *Struct. Eng. Mech.*, **49**(5), 597-618.

Jiang, S.Y., Du, C.B., Gu, C.S. and Chen X.C. (2014), "XFEM analysis of the effects of voids, inclusions and other cracks on the dynamic stress intensity factor of a major crac", *Fatigue Fract. Eng. Mater. Struct.*, **37**(8), 866-882.

Kim, J., Zi, G., Van, S, Jeong, M., Kong, J. and Kim, M. (2011), "Fatigue life prediction of multiple site damage based on probabilistic equivalent initial flaw model", *Struct. Eng. Mech.*, **38**, 443-457.

Kumar, S., Shedbale, A.S., Singh, I.V. and Mishra, B.K. (2015), "Elasto-plastic fatigue crack growth analysis of plane problems in the presence of flaws using XFEM", *Front. Struct. Civil Eng.*, **9**(4), 420-440.

Kumar, S., Singh, I.V. and Mishra, B.K. (2016), "New enrichments in XFEM to model dynamic crack response of 2-D elastic solids", *Int. J. Impact Eng.*, **87**, 198-211.

Kumar, S., Singh, I.V. and Mishra, B.K., (2014), "A multigrid coupled (FE-EFG) approach to simulate fatigue crack growth in heterogeneous materials", *Theor. Appl. Fract. Mech.*, **72**, 121-135.

Kumar, S., Singh, I.V. and Mishra, B.K., (2015), "A homogenized XFEM approach to simulate fatigue crack growth problems", *Comput. Struct.*, **150**, 1-22.

Kumar, S., Singh, I.V., Mishra, B.K. and Rabczuk, T. (2015), "Modeling and simulation of kinked cracks by virtual node XFEM", *Comput. Meth. Appl. Mech. Eng.*, **283**, 1425-1466.

Lam, K.Y., Zhang, J.M. and Ong, P.P. (1992), "A new integral equation formulation for the analysis of crack-inclusion interactions", *Comput. Mech.*, **10**, 217-229.

Lee, J., Choi, S. and Mal, A. (2001), "Stress analysis of an unbounded elastic solid with orthotropic inclusions and voids using a new integral equation technique", *Int. J. Solid. Struct.*, **38**, 2789-2802.

Melenk, J.M. and Babuška, I. (1996), "The partition of unity finite element method: Basic theory and applications", *Comput. Meth. Appl. Mech. Eng.*, **39**, 289-314.

Moës, N., Cloirec, M., Cartraud, P. and Remacle, J.F. (2003), "A computational approach to handle complex microstructure geometries", *Comput. Meth. Appl. Mech. Eng.*, **192**, 3163-3177.

Moës, N., Dolbow, J. and Belytschko, T., (1999), "A finite element method for crack growth without remeshing", *Int. J. Numer. Meth. Eng.*, **46**, 131-150.

Nishioka, T., Tokudome, H. and Kinoshita, M. (2001), "Dynamic fracture-path prediction in impact fracture phenomena using moving finite element method based on Delaunay automatic mesh generation", *Int. J. Solid. Struct.*, **38**, 5273-5301.

O'Hara, P., Duarte, C.A. and Eason, T. (2016), "A two-scale generalized finite element method for interaction and coalescence of multiple crack surfaces", *Eng. Fract. Mech.*, **163**, 274-302.

Ooi E.T., Shi M., Song C., Tin-Loi, F. and Yang, Z.J. (2012), "Dynamic crack propagation simulation with scaled boundary polygon elements and automatic remeshing technique", *Eng. Fract. Mech.*, **106**, 1-21.

Ooi, E.T. and Yang, Z.J. (2011), "Modelling dynamic crack propagation using the scaled boundary finite element method", *Int. J. Numer. Meth. Eng.*, **88**(4), 329-349.

Ooi, E.T., Song, C. and Tin, L.F. (2012), "Polygon scaled boundary finite elements for crack propagation modelling", *Int. J. Numer. Meth. Eng.*, **91**(3), 319-342.

Ortiz, M. and Pandolfi, A. (1999), "Finite-deformation irreversible cohesive elements for three-dimensional crack-propagation analysis", *Int. J. Numer. Meth. Eng.*, **44**(9), 1267-1282.

Osher, S. and Sethian, J.A. (1988), "Fronts propagating with curvature-dependent speed: algorithms based on Hamilton-Jacobi formulations", *J. Comput. Phys.*, **79**(1), 12-49.

Patton, E.M. and Santare, M.H. (1990), "The effect of a rigid elliptical inclusion on a straight crack", *Int. J. Fracture*, **46**, 71-79.

Rabczuk, T. and Belytschko, T. (2004), "Cracking particles: a simplified meshfree method for arbitrary evolving cracks", *Int. J. Numer. Meth. Eng.*, **61**, 2316-2343.

Rabczuk, T., Areias, P.M.A. and Belytschko, T. (2007), "A simplified mesh-free method for shear bands with cohesive surfaces", *Int. J. Numer. Meth. Eng.*, **69**, 993-1021.

Sharma, K., Singh, I.V., Mishra, B.K. and Shedbale, A.S. (2013), "The Effect of Inhomogeneities on an Edge Crack: A Numerical Study using XFEM", *Int. J. Comput. Meth. Eng. Sci. Mech.*, **14**(6), 505-523.

Shi, G.H. (1992), "Modeling rock joints and blocks by manifold method", *Proceedings of the 33th US Rock Mechanics Symposium*, New Mexico: Santa Fe.

Simpson, R. and Trevelyan, J. (2011), "A partition of unity enriched dual boundary element method for accurate computations in fracture mechanics", *Comput. Meth. Appl. Mech. Eng.*, **200**(1-4), 1-10.

Singh, I.V., Mishra, B.K. and Bhattacharya, S. (2011), "XFEM simulation of cracks, holes and inclusions in functionally graded materials", *Int. J. Mech. Mater. Des.*, **7**, 199-218.

Singh, I.V., Mishra, B.K., Bhattacharya, S. and Patil, R.U. (2012), "The numerical simulation of fatigue crack growth using extended finite element method", *Int. J. Fatigue*, **36**, 109-119.

Song, S.H. and Paulino, G.H. (2006), "Dynamic stress intensity factors for homogeneous and smoothly heterogeneous materials using the interaction integral method", *Int. J. Solid. Struct.*, **43**, 4830-4866.

Sukumar, N. and Prévost, J.H. (2003), "Modeling quasi-static crack growth with the extended finite element method, Part I: Computer implementation", *Int. J. Solid. Struct.*, **40**, 7513-7537.

Sukumar, N., Chopp, D.L., Moës, N. and Belytschko, T. (2001), "Modeling Holes and inclusions by level sets in the extended finite element method", *Comput. Meth. Appl. Mech. Eng.*, **190**(46-47), 6183-6200.

Wu, Z.J. and Wong, L.N.Y. (2013), "Modeling cracking behavior of rock mass containing inclusions using the enriched numerical manifold method", *Eng. Geol.*, **162**, 1-13.

Ye, C., Shi, J. and Cheng, G.J. (2012), "An eXtended Finite Element Method (XFEM) study on the effect of reinforcing particles on the crack propagation behavior in a metal-matrix composite", *Int. J. Fatigue*, **44**, 151-156.

Zhuang, X., Augarde, C. and Bordas, S. (2011), "Accurate fracture modelling using meshless methods, the visibility criterion and level sets: formulation and 2D modelling", *Int. J. Numer. Meth. Eng.*, **86**(2), 249-268.

Zhuang, X., Augarde, C. and Mathisen, K. (2012), "Fracture modeling using meshless methods and level sets in 3D: framework and modeling", *Int. J. Numer. Meth. Engng.*, **92**(11), 969-998.

CC